



Centrifuge modeling and numerical analysis of reservoir bank landslides triggered by a fast two-step drop in water level

Chaojun Jia^{1,2} · Fanlei Chen¹ · Qiang Zhang² · Jianyong GU³ · Jing Hu² · Hongjie Chen⁴ · Wei Cheng⁵

Received: 19 November 2022 / Accepted: 14 November 2023 / Published online: 27 November 2023
© Springer-Verlag GmbH Germany, part of Springer Nature 2023

Abstract

To meet flood control requirements, reservoir water levels undergo a two-step drop process before the rainy season. To examine the relationship between the deformation characteristics of the accumulation body and this water level drop, a large-scale centrifuge modeling study was conducted. The dropping scheme involved a second drop stage rate twice that of the first stage. The macroscopic deformation, pore pressure, and earth pressure change laws during the two-step drop were analyzed. Numerical simulations were also performed to assess the impact of water level rate on deformation and stability. The results showed that during reservoir impoundment, accumulation deformation was minimal. In the 1st drop stage, tensile cracks initially formed at the front edge and rapidly extended, creating a fault zone. As the fault zone collapsed, tensile cracks propagated toward the middle and back of the slope. In the 2nd drop stage, the slope continued to slide along the previously formed fault zone, albeit with reduced intensity. Vertical compaction in the middle and rear sections contributed to stabilizing crack expansion. Pore pressure exhibited hysteresis during reservoir impoundment but gradually weakened in each drop stage. Earth pressure on the leading edge underwent significant changes in each stage, with the highest intensity observed during the first drop stage in the middle and rear sections. The water level drop rate triggering slope instability ranged from 0.7 to 1.5 m/d in the 1st drop stage. Deformation and failure demonstrated a progressive weakening pattern from the front to the rear.

Keywords Centrifuge modeling · Numerical simulation · Failure mechanism · Two-step drop · Drop rate

Introduction

Reservoir bank landslides are among the most crucial issues faced during the construction and operation of hydropower projects (Jia et al. 2021). The trigger factors and failure mechanism of reservoir landslides are difficult to study, especially the long-term deformation evolution trend under

the repeated rise and fall of water levels. Therefore, catastrophic events caused by reservoir landslides are widespread, such as the left bank landslide of Vajont Reservoir in Italy (Paronuzzi et al. 2013), the Tangyanguang landslide of Zhexi Reservoir in Hunan Province, China (Huang et al. 2017), and the Qianjiangping landslide in the Three Gorges Reservoir area, China (Wang et al. 2004, 2008). According to statistics, most of the reservoir bank landslides occurred during the sudden drop in reservoir water level (Jones et al. 1961; Riemer 1992). Therefore, it is necessary to study the influence of the fast drop process on the deformation and stability of the reservoir slope.

Many reservoir bank landslides triggered by the change in water level were reported all over the world. For example, the Xintan landslide occurred in Hubei Province, China, in 1985 (Chen et al. 2021), and the Kuzulu landslide occurred in Sivas, Turkey, in 2005 (Yilmaz et al. 2006). Scholars have studied the reactivation of slopes under reservoir water level changes using field monitoring data analysis, physical model tests, laboratory mechanical tests, and numerical

✉ Qiang Zhang
zhangq@iwhr.com

¹ School of Civil Engineering, Central South University, Changsha 410075, China

² State Key Laboratory of Simulation and Regulation of Water Cycle in River Basin, Beijing 100048, China

³ Collage of Civil Engineering & Architecture, China Three Gorges University, Yichang 443002, China

⁴ Huaneng Lancang River Hydropower Inc., Kunming 650214, Yunnan, China

⁵ PowerChina Kunming Engineering Corporation Limited, Kunming 650000, Yunnan, China

simulation methods (Pinyol et al. 2012; Schuster 1979; Tian et al. 2022; Trzhtsinskii 1978; Yin et al. 2016). The deformation properties of landslides can be immediately studied when combined with monitoring data, allowing for the creation of pertinent geomechanical models (Highland and Bobrowsky 2008). Laboratory tests can be used to analyze the mechanical properties of the landslide body and sliding surface and to retrieve the macroscopic evolution characteristics and deformation mechanism of the landslide. Laboratory physical models and numerical simulations can simulate the influence of water on slope stability with fluid–solid coupling analysis (Miao et al. 2018). Compared with the aforementioned research methods, the geotechnical centrifuge modeling test can precisely duplicate the stress field and reveal the deformation and damage process (Wang et al. 2022, 2023). It is used more frequently in the study of slope deformation (Idinger et al. 2011). For example, rainfall-induced landslides (Eab et al. 2014), the destabilization process of rocky landslides (Liu et al. 2022), the damage mechanism of loess landslides (Zhang et al. 2019), deformation process of submarine landslides (Zhang and Askarinejad 2019), and the effect of anti-slip pile (Zhou et al. 2019) are well investigated. Askarinejad and Springman (2015) studied the hydro-mechanical response of a 38° vegetated silty sand slope triggered by heavy rainfall. Eab et al. (2014) investigated the effect of the root system on slope stability by designing a rainfall simulator in a centrifuge model chamber. Gue et al. (2010) simulated underwater landslides under different centrifugal accelerations, measured the slip velocity, and monitored the pore water pressure inside the sliding bed. Wang et al. (2020) obtained the forces acting on the submarine landslide impact pipeline inside a drum centrifuge. However, there are few studies on centrifuge modeling tests for long-term evolution characteristics of landslides under fast water level drops. Moreover, the sudden drop in water level can actually be subdivided into two stages. Reservoirs reduce the water level to generate electricity during operation time, and such reduction process is gentle. At the same time, it also needs to rapidly lower water levels to vacate capacity when the rainy season comes to meet flood control needs. Therefore, the reservoir water level drop rate is not consistent before and after the actual reservoir water scheduling scheme, and the drop rate becomes faster at the later stage of reservoir water level plunge with the approach of flood season. The existing studies only consider the reservoir level drop at one rate (Miao et al. 2018, 2022), which is different from the real reservoir scheduling situation.

In this paper, a set of water level variation systems was developed for centrifuge using LXJ-4–450 geotechnical centrifuge of China Institute of Water Resources and Hydropower Research (IWHR), and a two-step water level drop process was conducted to investigate the deformation properties of the accumulation body slope. The influence of the

reservoir water level drop rate on the slope deformation and stability is analyzed with a numerical simulation method. The deformation pattern of the slope and the mechanism of gradual stabilization of the middle and rear parts of the slide are revealed, which provides some reference basis for predicting the long-term stability of the reservoir bank slope.

Study area

The typical reservoir bank landslide that occurred in early June 2019 in Huangdeng Reservoir triggered by a two-step water level drop is selected for the investigation. Huangdeng Hydropower Station (Fig. 1a) is located in Lanping County, Yunnan Province, and is the fifth stage of the hydropower gradient development program in the upper reaches of the Lancang River from Gushui to Miaowei River section (Dong et al. 2018). In early June 2019, dozens of landslides occurred during the two-step drop in the reservoir water level. According to the field investigation report by the reservoir operation manager, there were 26 landslides triggered on both sides of the reservoir area (Fig. 1a), with the mass volume ranging from hundreds of thousands to millions of cubic meters. Some of the reservoir sections have multiple ground cracks and slides, and local bank deformation has caused interruptions in the road along the reservoir. The hydrological information in Fig. 1b shows that the water level has undergone a successive two-step drop process with low rainfall intensity. Therefore, we intended to analyze the deformation mechanism of landslides under the action of a two-step drop of reservoir water level to understand the deformation behavior of reservoir bank slopes and realize landslide disaster prevention and control.

Centrifuge modeling test

Test equipment

The LXJ-4–450 geotechnical centrifugal testing machine of IWHR (Du et al. 1992) is adopted to conduct the tests. The main engine of the test system is composed of the turntable, the crane, the rotating arm, the counterweight basket, the model basket, and the control system (Fig. 2). The main engine features a double swing, symmetrical arms, and double hanging baskets, resulting in excellent dynamic balance and model test accuracy. The parameters of this test system are shown in Table 1.

Centrifuge kinematics

Due to the equivalence of inertial forces to Newtonian gravity, the gravitational force exerted by the prototype in

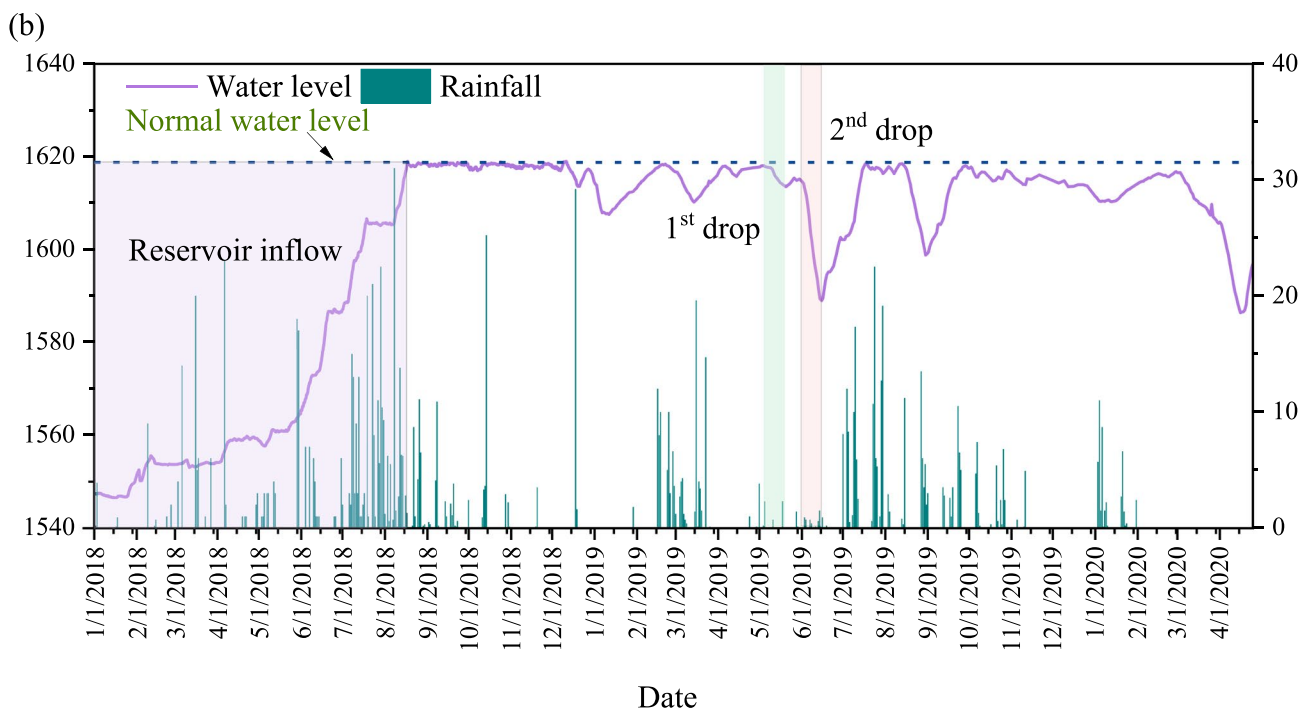
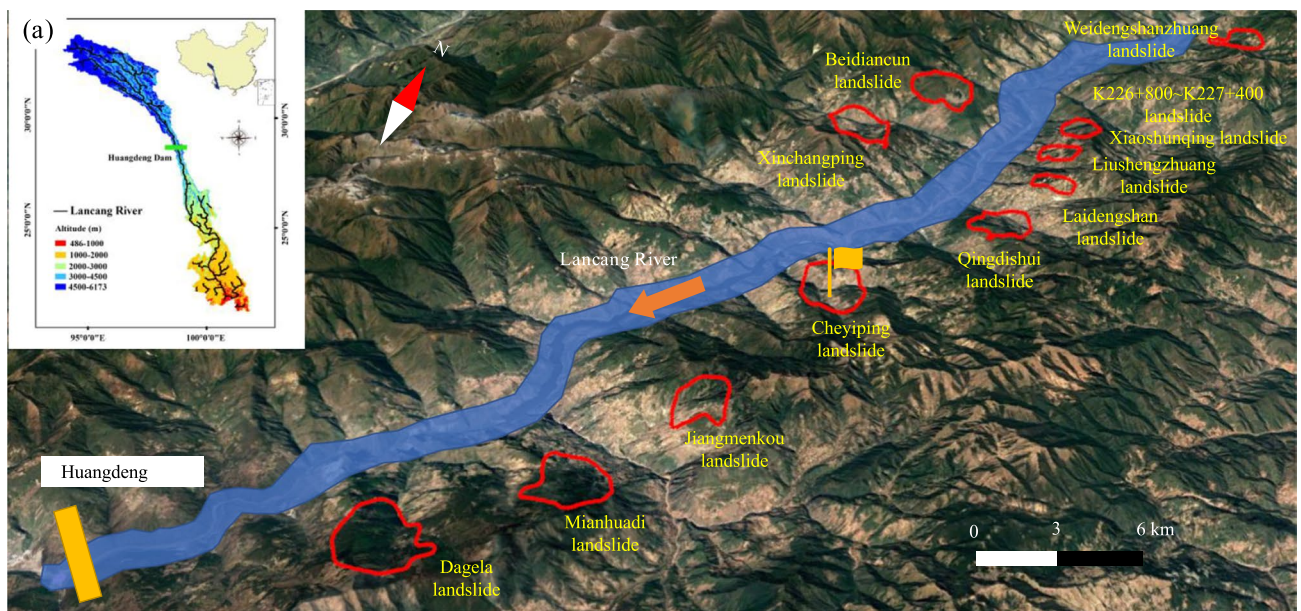


Fig. 1 A Location of the landslides (early June 2019) induced by the change of reservoir water level in Huangdeng reservoir and (b) water level variation and rainfall in the reservoir area

a constant gravity field ($g = 9.8 \text{ m/s}^2$) and the centrifugal inertial force exerted by the model in a centrifugal field agree in their physical effects. The inherent properties of the material are mainly influenced by electromagnetic forces, and the effects of gravity or centrifugal forces are negligible. Therefore, the properties of the soil material do not change under the centrifugal force field. The centrifugal test simulates gravity by centrifugal force, which

in turn raises the self-weight of the landslide model to the prototype level.

Figure 3 shows the overburden stress of a slope prototype and the model with a $1/N$ scale placed in a $1g$ gravity field and an Ng centrifugal force field, respectively. Under the centrifugal acceleration of Ng , the linear dimension ratio of the prototype to the model is N . If the directional error of the centrifugal acceleration of Ng is excluded, the

Fig. 2 LXJ-4-450 geotechnical centrifuge of China Institute of Water Resources and Hydro-power Research

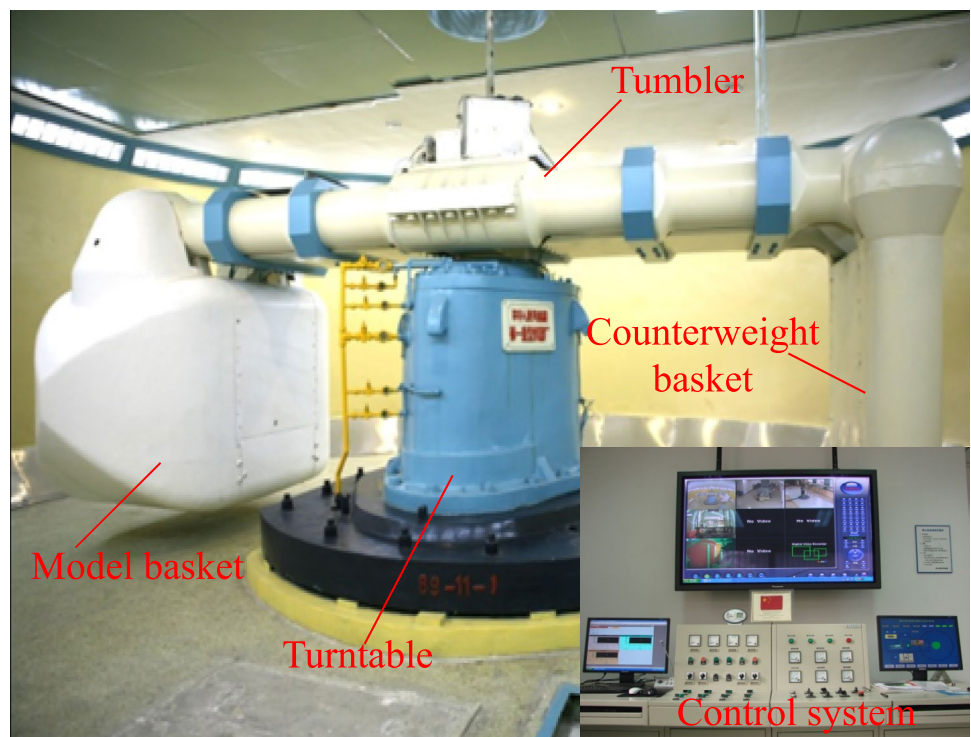


Table 1 Parameters of LXJ-4-450 type geotechnical centrifuge system

Main technical parameters	Parameter value
Maximum capacity	450 g·t
Effective radius	5.03 m
Acceleration range	10~300 g, speed stability 0.5%/F.S., 12 h
Effective load	Maximum payload 3 t at 100 g, maximum payload 1.5 t at 300 g
Hanging basket volume	$L \times W \times H = 1.5 \text{ m} \times 1.0 \text{ m} \times 1.5 \text{ m}$
Drive motor power	DC motor for drive, motor power is 700 KW

overburden stresses of the prototype and the model are the same. The centrifugal coordinate system after scaling is shown in Fig. 4a, and the acceleration component at point A in the centrifugal model in the local coordinate system is shown in Fig. 4b. When the centrifugal acceleration lifts to the set speed and keeps that speed continuously rotating, the angular acceleration is $d^2\theta/dt^2 = 0$, and the radial velocity of point A also tends to zero ($dr/dt \approx 0$). At this time, the centrifugal acceleration borne by the model can be expressed as $r(d\theta/dt)^2$. Thus, an artificial model force field is formed.

The three similar conditions required for the centrifugal model test are similar size, similar force, and similar physical quantities of materials (Ge et al. 2017). The first

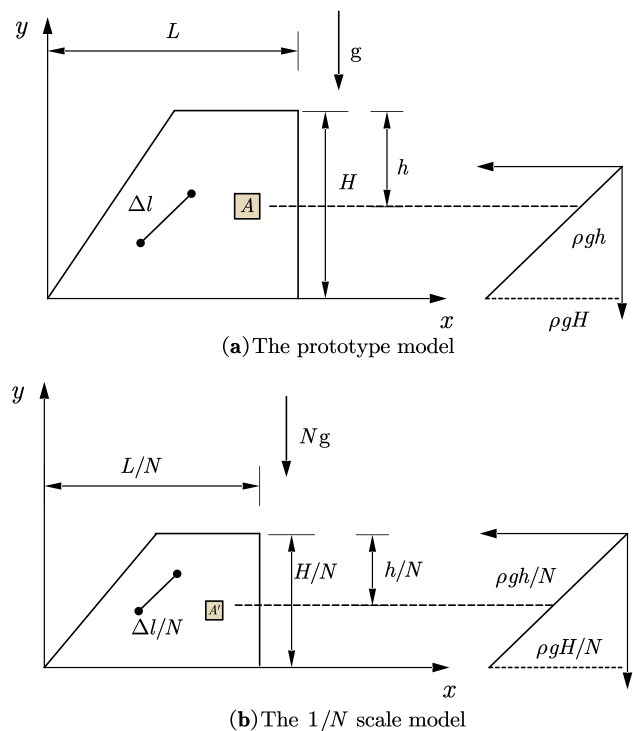


Fig. 3 Overburden stresses for the slope prototype and the model scaled to (a) 1/N placed in the 1 g gravity field and (b) the Ng centrifugal force field, respectively

Fig. 4 Acceleration components of point A in the centrifugal model in (a) the centrifugal coordinate system and (b) the local coordinate system after scaling 1/N times

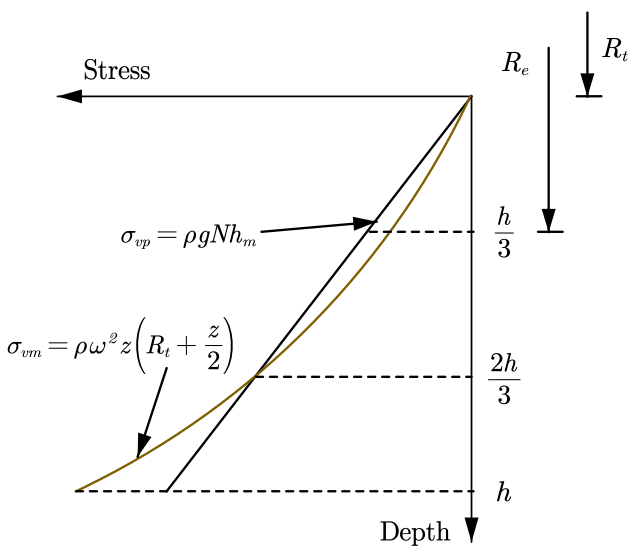
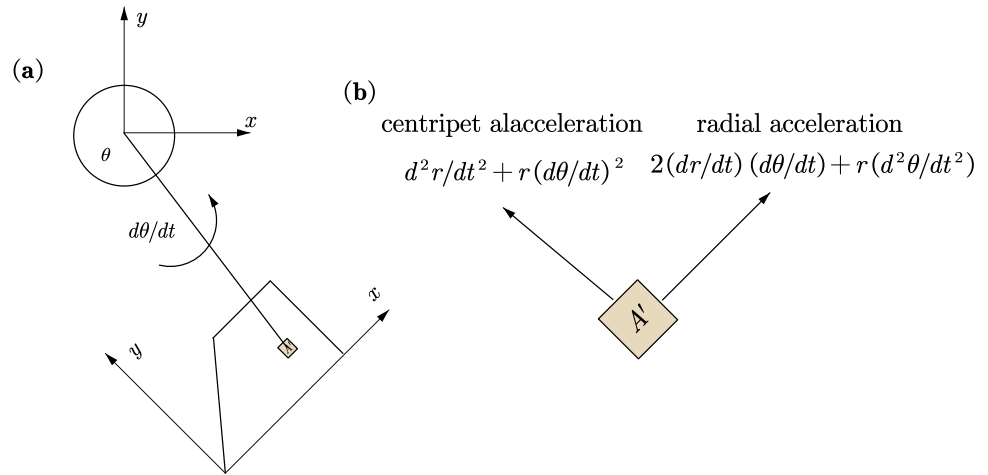


Fig. 5 Prototype vs. centrifuge model vertical stress versus depth

two similarity conditions make the model reflect the slope prototype stress–strain relationship, and the last similarity condition ensures that the stress–strain relationship between the model and the prototype is consistent.

Due to the different centrifugal forces on the model in the radial direction of the centrifuge, the stress between the model and the prototype is also slightly different. Assume that the effective turning radius of the centrifuge is R_e , as shown in Fig. 5. Then, we have

$$Ng = \omega^2 R_e \tag{1}$$

where ω is the angular acceleration of the centrifuge rotating arm. The prototype vertical stress σ_{vp} is

$$\sigma_{vp} = \rho g h_p = \rho g N h_m \tag{2}$$

where h_p and h_m are the depth of the prototype and centrifuge model, respectively.

Assuming that the distance between the top surface of the slope model and the axis of rotation is R_t , the vertical stress σ_{vm} of the slope model is

$$\sigma_{vm} = \rho \omega^2 \int_0^z (R_t + z) dz = \rho \omega^2 z \left(R_t + \frac{z}{2} \right) \tag{3}$$

Assuming that the model vertical stress $z = h_i$ is the same as the prototype vertical stress, it can be known from Eqs. (1), (2), and (3) that

$$R_e = R_t + 0.5h_i \tag{4}$$

When $z < h_i, \sigma_{vp} > \sigma_{vm}$. When $z > h_i, \sigma_{vp} < \sigma_{vm}$. Assuming $r_u = \max[(\sigma_{vp} - \sigma_{vm})/\sigma_{vp}]$, it has $r_o = \max[(\sigma_{vm} - \sigma_{vp})/\sigma_{vp}]$. If $r_u = r_o$, it follows that

$$h_i = \frac{2}{3}h_m \tag{5}$$

$$r_o = r_u = \frac{h_m}{6R_e} \tag{6}$$

$$R_e = R_t + \frac{h_m}{3} \tag{7}$$

To control the stress error to a minimum, the effective radius of the centrifuge should be selected from the distance from the rotating shaft to the 1/3 height position of the centrifugal model. The geotechnical centrifuge at the IWHR has a maximum radius of $r_{max}=5.03$ m and the maximum height of 0.9 m. Therefore, the stress error is

$$\max(r_o) = \max(r_u) = \max\left(\frac{h_m}{6R_e}\right) = \frac{0.9}{6(5.03 - 0.6)} \approx 3.39\% \tag{8}$$

The maximum stress error of this geotechnical centrifuge is $3.39\% < 5\%$, which is within the allowable range of stress error.

The physical model test requires a specific similarity criterion to establish correspondence with the prototype. The similarity criterion for the centrifugal test makes this research method uniquely advantageous. The similarity criterion for physical quantities commonly used in centrifuge modeling tests is shown in Table 2 according to the research of Fuglsang and Ovesen (1988).

Mechanical parameters of the model material

According to the *in-situ* survey, the bedrock beneath the landslides in the reservoir bank is predominantly slate, sandstone, or andesite, which is weakly permeable. The upper part of the slope mass is covered with an accumulation body, as the bedrocks are with high strength and stiffness. For simplicity, the model sliding bed in this centrifugal model test is regarded as an impermeable body. The sliding bed and the water input tank are chosen to be integrated to meet the test requirements after considering the size of the model test box and the needs of the water supply and drainage system.

In-situ water injection tests and laboratory permeability tests were conducted to determine the coefficient of saturated permeability of the accumulation body. The permeability coefficient of the Quaternary loose accumulation is $k = 4.5 \times 10^{-4}$ cm/s, which is weakly permeable according to the Chinese Standard SL386-2007 (2007). Therefore, the corresponding permeability and strength requirements can be met by remolding the material of the sliding mass.

The sliding mass (accumulation body) used in the test was directly taken from the Huangdeng Reservoir bank, and the particle size of the soil varies from 50 to 500 mm. According to the Chinese test specification known as the Code of Geotechnical Centrifuge Model Tests (DL/T 5102-1999), it entails using coarse grains with the largest size permitted in a centrifuge test to substitute oversized coarse grains with an equivalent number of alternative-diameter particles, maintaining the original granule content and modifying the inhomogeneity of the earth material. The more commonly used method is the equivalent substitution method (Zhao et al. 2019). The soil samples were naturally air-dried and passed through a geo-sieve, and the equation for calculating the particle size content of each group after substitution is as follows:

$$P_i = \frac{P_{oi}P_5}{P_5 - P_{dmax}} \tag{9}$$

where P_i is the content of a particle size group after substitution, %; P_5 is the content of the soil with particle size greater than 5 mm, %; P_{dmax} is the content of super-sized soil particles, %; P_{oi} is the content of particles of the original gradation group, %. After removing the super-sized soil particles from the soil samples taken from the reservoir bank, the particle size gradation curve of the experimental model soil is obtained, as shown in Fig. 6.

Before the centrifugal modeling tests, the soil samples with different moisture content were prepared, and direct shear tests were carried out on these soil samples. On this basis, different contents of stone were mixed, and the permeability coefficient was determined by the laboratory constant head permeability tests. Finally, a model material that is similar to the actual parameters of the sliding body is obtained. This test was equipped with 208 kg of slide body with a natural moisture content of 12%, and its physical and mechanical parameters are shown in Table 3.

Construction of the model

The purpose of this centrifugal modeling test is to study the deformation characteristics and failure mechanism of

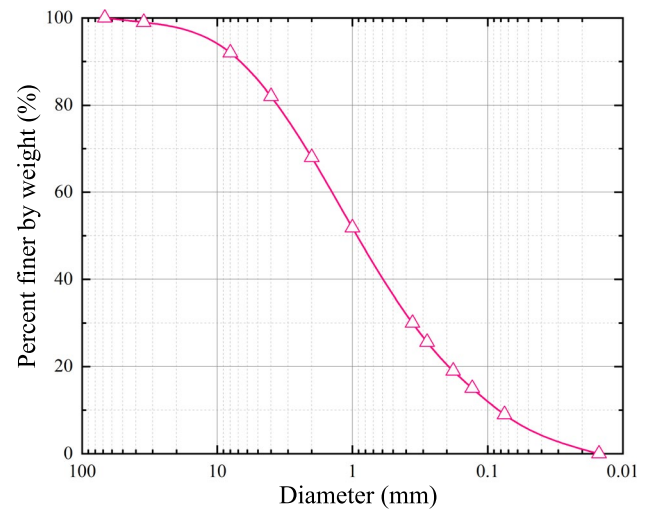


Fig. 6 Particle size gradation curve of the sliding mass in the centrifugal modeling tests

Table 2 Guidelines for similarity of physical parameters commonly used in centrifuge modeling tests

Physical quantities	Acceleration	Length	Area	Volume	Stress	Strain	Weight
Scale factor	N	$1/N$	$1/N^2$	$1/N^3$	1	1	$1/N^3$
Physical quantities	Porosity ratio	Viscosity	Force	Torque	Density	Time (power)	Time (seepage)
Scale factor	1	1	$1/N^2$	$1/N^3$	1	$1/N$	$1/N^2$

Table 3 Physical and mechanical parameters of the landslide deposit used in the model tests

Density (g/cm ³)	Water content (%)	Cohesion (kPa)	Friction angle (°)	Permeability coefficient (10 ⁻⁵ cm/s)	Liquid limit (%)	Plastic limit (%)	Plasticity index
1.81	12	31.7	22.9	3.40	23.2	12.4	15.86

the reservoir bank slope triggered by a two-step drop in water level. Considering the prototype scale of the landslide in the Huangdeng Reservoir bank deformation section, combined with the loading capacity of the geotechnical centrifuge and the size of the model box, the maximum centrifugal acceleration of this centrifugal test is determined to be 70 g. To reduce the scale effect of the model as much as possible, a model box with a larger size was selected. The size of the model box is 1450 mm (length), 3500 mm (width), and 31,000 mm (height), and the wall thickness is 50 mm. According to the engineering geological profile of the typical landslide in the reservoir area,

the size of the landslide test model is 1035 mm (length), 400 mm (width), and 690 mm (height), as shown in Fig. 7.

According to the pre-designed test plan, the monitoring system mainly includes pore pressure transducers (diameter 5 mm, range of 250 kPa, 300 kPa, and 400 kPa, accuracy 0.1%FS) (Fig. 7c), micro-earth pressure sensors (diameter 8 mm, range of 500 kPa, 1000 kPa, and 2000 kPa) (Fig. 7d). Among them, pore pressure transducer P1 is arranged at the front edge of the slope to monitor the water level change. To accurately monitor the pore pressure at different positions inside the slope, seven pore pressure sensors were embedded in three layers in the slope, as shown in Fig. 7a. Three

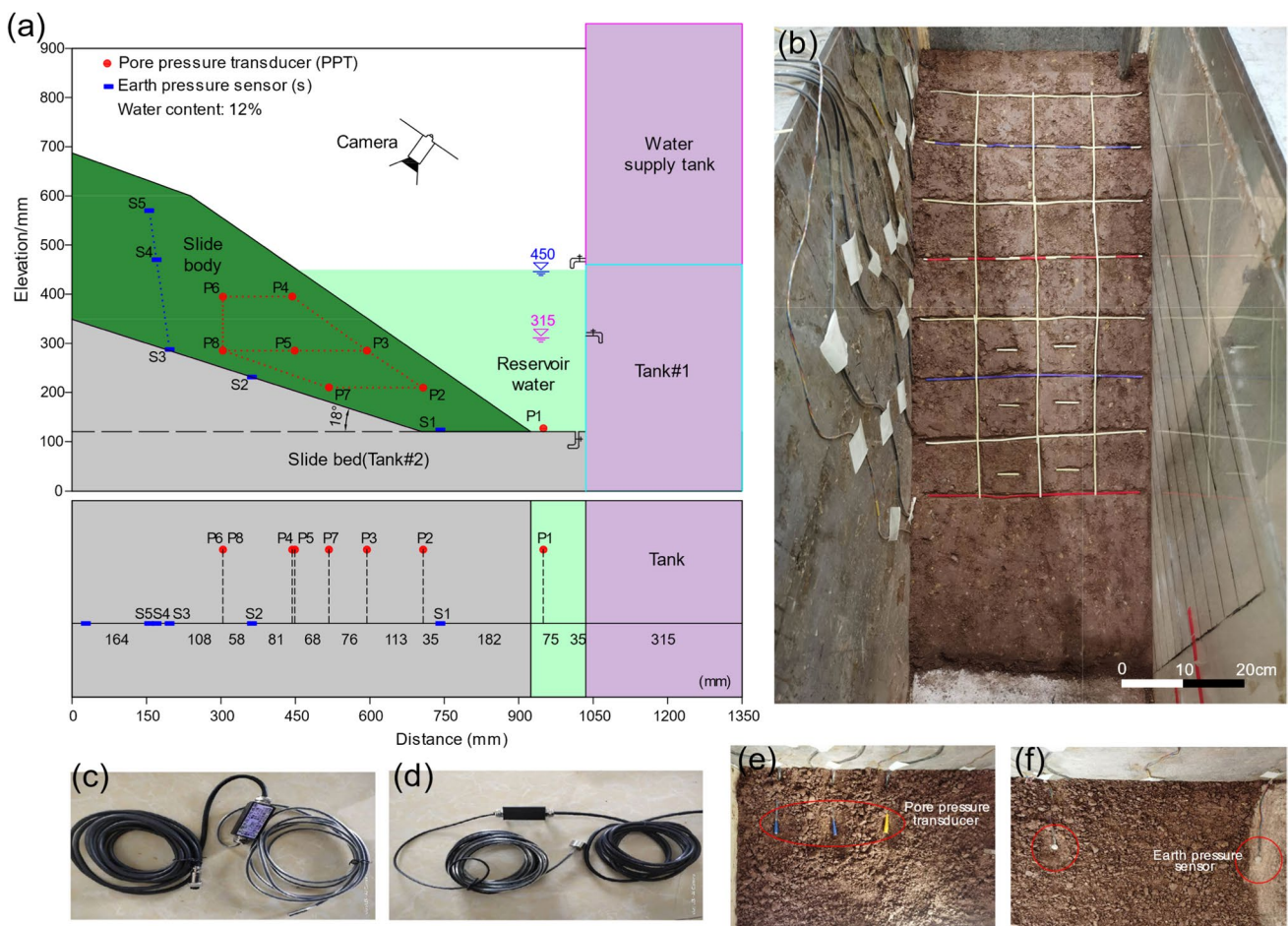


Fig. 7 Centrifuge modeling test layout: (a) layout of sensors and the size of the model box; (b) photo of slope surface; (c) pore pressure transducer; (d) earth pressure sensor; and (e) and (f) arrangement of the sensors

and two earth pressure sensors were embedded in the vertical direction and the middle and upslope part along the sliding belt to monitor the change of the earth pressure on the sliding surface. In addition, three cameras are arranged on the top of the leading edge, the top of the trailing edge, and the side of the model box to capture the deformation and the water level change during the centrifugal modeling tests (Fig. 7a). At the same time, the slope surface is meshed to monitor the deformation of the slope surface macroscopically (Fig. 7b).

Centrifuge modeling test results and analysis

Macroscopic deformation

In this experiment, the process of one-step reservoir water rises, and two-step water level drops were designed according to the reservoir operation scheme in early June 2019, as shown in Fig. 1. By comparing the high-definition camera images of the test process, the complete macroscopic deformation evolution process of the landslide can be obtained. The variation of the acceleration and the water level is shown in Fig. 8. The complete test process can be divided into three stages: impoundment stage ①, 1st drop stage ②, and 2nd drop stage ③. Starting from the 2520 s in the timeline, keep the acceleration constant at 70 g. The water level starts to rise and submerges the foot of the slope at the rate of 9.8 cm/min. The final water level elevation is 33 cm at this stage. Subsequently, two consecutive water level drops are arranged. The water level rose at a rate of 9.8 cm/min for 202 s. The water level dropped from the highest level of 450 mm to the low level of 315 mm, and the water level plummeting rate was 3.4 cm/min, lasting 238 s. The water level drops from 315 mm at low level to 120 mm at zero level. At this point, all the water in the reservoir is emptied, and the water level plummets at a rate of 7.3 cm/min, lasting 160 s. The deformation characteristics of the landslide surface at each stage are shown in Fig. 9.

Stage ①: From the 2520th second, the water level rises rapidly to the highest water level of 33 cm. At this time, the acceleration remains unchanged at 70 g. At the 2670th second, the slope accumulates a settlement deformation of about 0.3 mm, which belongs to the normal consolidation settlement of the soil during the impoundment process of reservoir water (Fig. 9a, b). Generally speaking, there is no obvious sliding deformation of the sliding body at this stage.

Stage ②: At 4560th second, the water level drops for the first time. Slight creep and settlement deformation occurs on the front edge of the slope, and tension cracks grow in the middle and rear parts. It is worth noting that seepage has a strong effect on slope erosion during the period from 4650 to 4830 s when the reservoir water level drops from 25.7 to 20.6 cm. The slope has undergone obvious deformation, which is manifested as the overall creep deformation of the front edge and the staggering collapse under the transverse crack, forming a fracture zone with a width of about 25 to 35 mm, as shown in Fig. 9c. The cracks in the middle and rear part continue to expand and develop. At this stage, the deformation triggered by the fast change of water level is the largest at the front edge of the slope, followed by the middle part, and the smallest deformation in the rear part.

Stage ③: After 6240 s, the water level drops again. Its decline rate is about twice as fast as that stage ②. During the period from 6300 to 6480 s, due to the low water level elevation, the intensity of seepage erosion is weakened, which mainly occurs in the shallow soil body in the sudden change of the water level on the front edge. It is manifested as the continuous expansion of the fracture zone. After the test, the depth of the front edge of the slope is about 30 to 60 mm, and the middle is deeper. In general, an overall slip of the slope occurs, as shown in Fig. 9d. A multi-level slip surface is formed, and the cumulative width of the cracks at the trailing edge of the slope is about 5 mm, and no obvious large deformation occurs in this area. The final shape of the landslide is shown in Fig. 10.

Fig. 8 Deformation stage division of the centrifuge modeling test

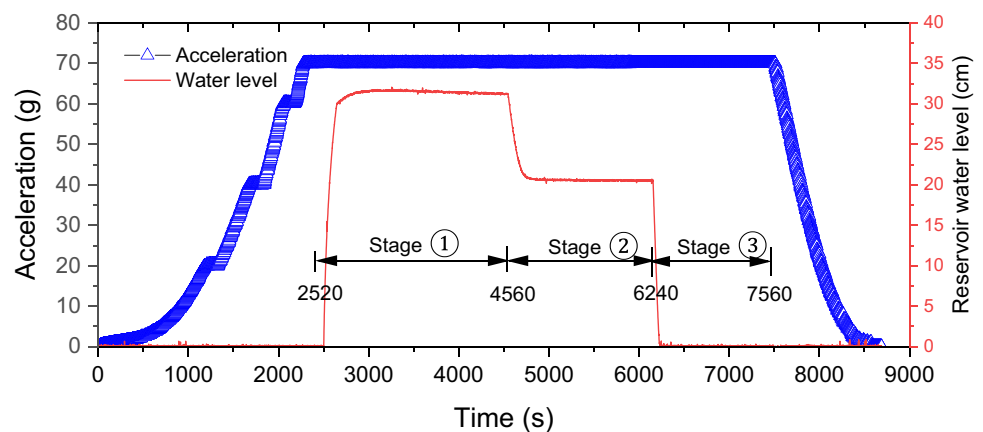


Fig. 9 Deformation characteristics of landslide slope surface at (a) step acceleration stage; (b) impoundment to the maximum water level stage; (c) after the 1st drop stage; and (d) after the 2nd drop stage

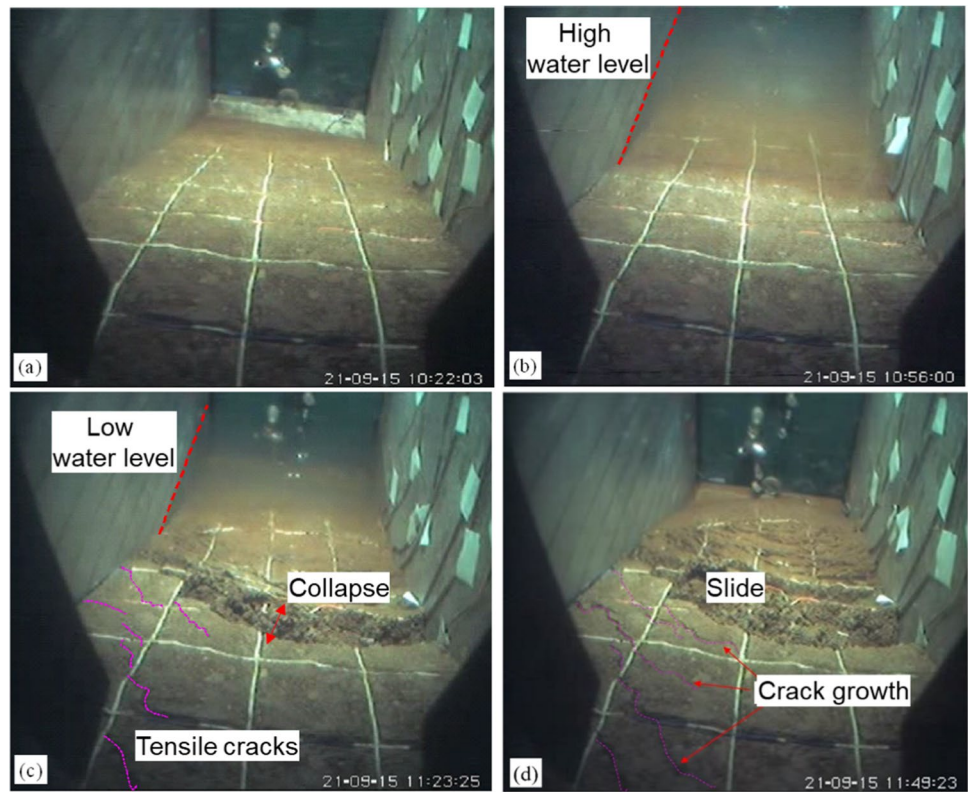
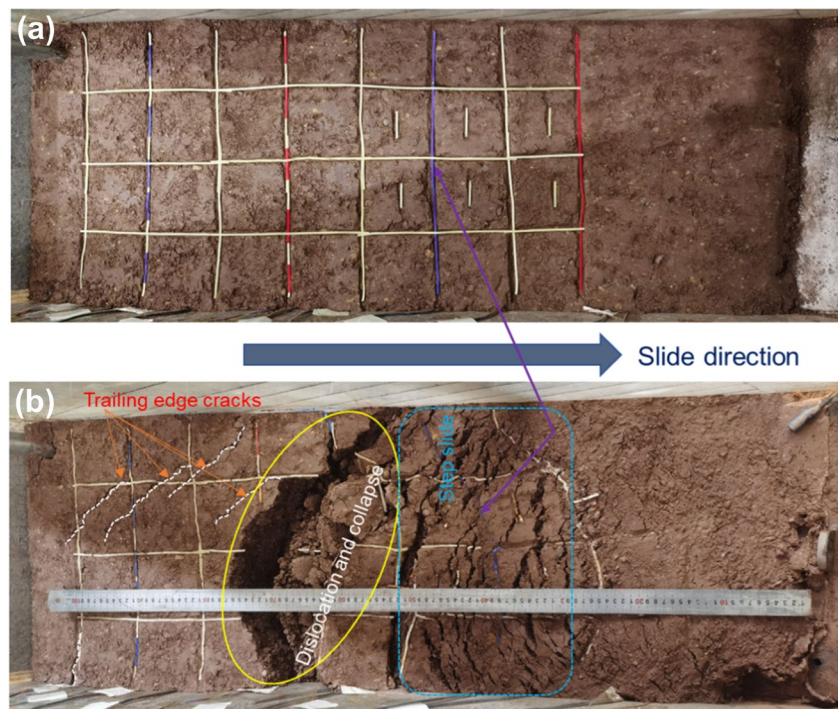


Fig. 10 Final form of landslide deformation and damage and deformation characteristics of landslide leading edge slope surface



Pore pressure variation

The time axis of the preset plan is changed from 2520 to 0 s in the analysis of pore pressure variations to improve

analysis and explanation because there is no reservoir water infiltration in the slope during the accelerated operation stage of the centrifuge. Since the response time of the pore pressure sensors buried at different heights inside the slope

is inconsistent with the rise of the reservoir water level, the sensors can be divided into three layers to analyze the variation of pore pressure (Fig. 11). The lower pore pressure sensor is P2, P7 from outside to inside, the middle pore pressure sensor is P3, P5, P8 from outside to inside, and the upper pore pressure sensor is P4, P6 from outside to inside, as shown in Fig. 7.

When the water level of the reservoir rises to 14 cm, it triggers an increase in pore pressure at P2, indicating the infiltration of reservoir water in that area. Specifically, when the water level exceeds P2 by approximately 5 cm, it infiltrates the location of P2. Once the water level reaches 23 cm, the pore pressure at P7 increases, while the time delay for P2 is approximately 54 s. Subsequently, P2 and P7 initially exhibit exponential growth, followed by a deceleration during the later stage of impoundment. This phenomenon occurs because, during the initial stage of impoundment, the gradual formation of the reservoir water infiltration channel results in a steep increase in pore pressure, which subsequently diminishes as the water volume in the supply tank decreases. After adding water, the pore pressure at P2 is higher than at P7. This discrepancy arises because the reservoir water infiltrates toward P7 along the infiltration path of P2, driven by the centrifugal force field. Moreover, the greater distance between P7 and the reservoir water leads to reduced infiltration and lower pore pressure.

During the 1st drop, there is a lag of 32 s between the response of pore pressure at P2 and P7 and the reservoir water level. However, the pore pressure at P2 is delayed by 16 s and at P7 by 18 s during the 2nd drop stage. This occurs because the 1st drop stage creates a seepage channel for the 2nd drop. Furthermore, as the drop rate of reservoir water increases in the 2nd drop stage, the slope deformation

becomes more pronounced. It shows that the response lag of pore pressure inside the slope is stronger in the 1st drop stage than in the 2nd drop stage. Between 2312 and 3720 s, as well as between 3826 and 5040 s, the water level remained unchanged while the pore pressure at P2 gradually decreases. The decline rate in P2 during the 1st drop stage is higher than that in the 2nd drop stage, whereas P7 remains relatively stable during these two periods. This indicates that the shallow infiltrated water continues to seep under its own weight. The initial infiltration volume is substantial, while the subsequent internal secondary infiltration diminishes significantly due to the formation of infiltration channels. However, the deep infiltration process of the landslide is not readily apparent. During the deceleration and shutdown of the centrifuge, the pore pressure gradually decreases, and the landslide deformation is completed at this time.

When the water level rises to 28 cm, the pore pressure at P3 begins to increase, with a lag of approximately 59 s compared to P7. Pore pressure at P5 gradually increases at 176 s, lagging behind P3 by about 27 s. Meanwhile, the water level has reached and stabilized at 30 cm, which is 12 cm above its original position. Upon reaching a water level of 31 cm, the pore pressure at P8 begins to respond, while the lag for P5 is approximately 50 s. After adding water, the pore pressure at P3 is the largest, followed by P5, and P8 exhibits the lowest pressure. This occurs because the reservoir water gradually depletes as it flows successively through P3, P5, and P8 under the influence of the centrifugal force field. Even after the reservoir water reaches its maximum level, the pore pressure continues to slowly decrease, suggesting a downward migration of water. At 2169 s, the reservoir water level is still dropping, while both pore pressures at P3 and P5 exhibit slight increases. The increase in P5 is higher

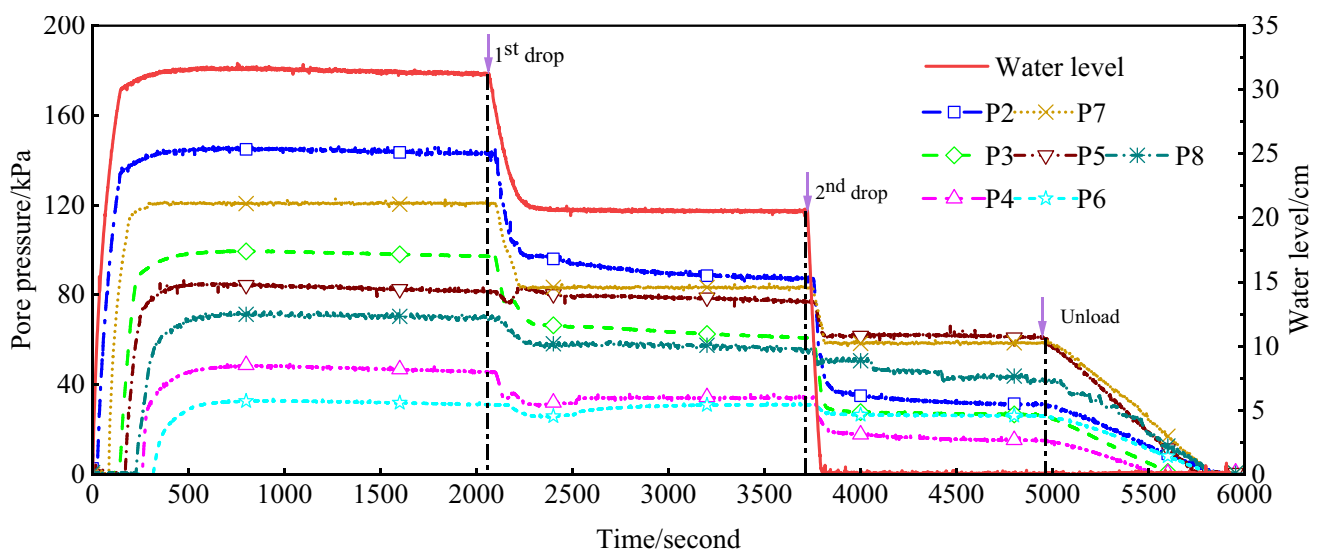


Fig. 11 Pore pressure variation curves inside the slope during the complete centrifuge modeling stage

than that in P3, although this difference is less prominent during the 2nd drop stage. This is because the groundwater within the landslide body migrates under the action of hydrodynamic pressure, infiltrating into P3 and P5. Following the 1st drop stage, the water level reaches 19.5 cm, a mere 3 cm above that of P3 and P5. Consequently, there is no infiltration of reservoir water into P3 and P5 during the subsequent second sudden drop. It shows that the migration of deep groundwater is more pronounced compared to shallow groundwater. Throughout the 2nd drop, P8 exhibits gradual decreases, indicating deformation and slippage at this specific site.

When the water level reaches 32 cm, the pore pressure at P4 begins to increase, with a lag of approximately 36 s compared to P8. The reservoir water level is merely 5 cm above the elevation of P4, resulting in a relatively minor increase. When the water level reaches its maximum height of 33 cm, the pore pressure at P6 begins to respond, with a lag of about 32 s compared to P8. Water primarily infiltrates P4 and subsequently reaches P6, resulting in a slightly lower increase compared to P4. After the 1st drop stage, both pore pressures at P4 and P6 exhibit gradual increase, with P6 showing a higher rate of increase than P4. It shows that the infiltration process is slower in the middle and rear part of the slope, while its deep position is slower. The pore pressures P4 and P6 above the water level continue to decline during the 2nd drop stage, indicating that with the drop of the reservoir water level, local deformation cracks and collapse of the landslide occur, resulting in a continued decrease in the upper pore pressure. At the same time, the water level of the reservoir has been emptied after the 2nd drop, while P4 is still slowly falling. It shows that the shallow soil above the landslide is still undergoing creep deformation at this time.

In summary, the pore pressure monitoring data show that the slope response has a certain degree of hysteresis

compared with the rising reservoir water level. The formation of seepage channels weakens this hysteresis following the 1st drop stage, and the hysteresis becomes less apparent after the 2nd drop stage. Consequently, the landslide response accelerates after the reservoir water undergoes two-step sudden drops, with the deep groundwater being more significantly affected by the dynamic water pressure compared to the shallow groundwater. In the 2nd drop stage, the descent rate intensifies, resulting in a decreased rate of pore pressure reduction. Additionally, the pore pressure declines in the shallow layer, which is greater than that in the deep layer. The variation in pore pressure in the lower part of the slope is 2 to 5 times higher than that in the middle and upper part, indicating its heightened sensitivity to the reservoir water.

Earth pressure variation

To monitor the variation in earth pressure at the potential bottom sliding surface of the slope, as well as the middle and rear sections, three micro-earth pressure sensors (S1, S2, and S3) are arranged along the potential bottom sliding surface of the slope model. Additionally, two miniature earth pressure sensors (S4 and S5) are vertically arranged in the middle and rear sections, as shown in Fig. 7. The monitoring curves of each earth pressure sensor during the test are shown in Fig. 12.

(1) Deep bottom slip surface earth pressures (S1, S2, and S3).

The monitoring data of the earth pressure sensors S1 to S3 exhibit synchronous linear increases with acceleration. Upon reaching an acceleration of 70 g, S3 registers the highest earth pressure, followed by S2, and finally, S1, with the lowest reading. This is because S3 is located in the deepest part of the slope body close to the sliding bed and has less deformation. S2 is shallower than S3, and S1 is the

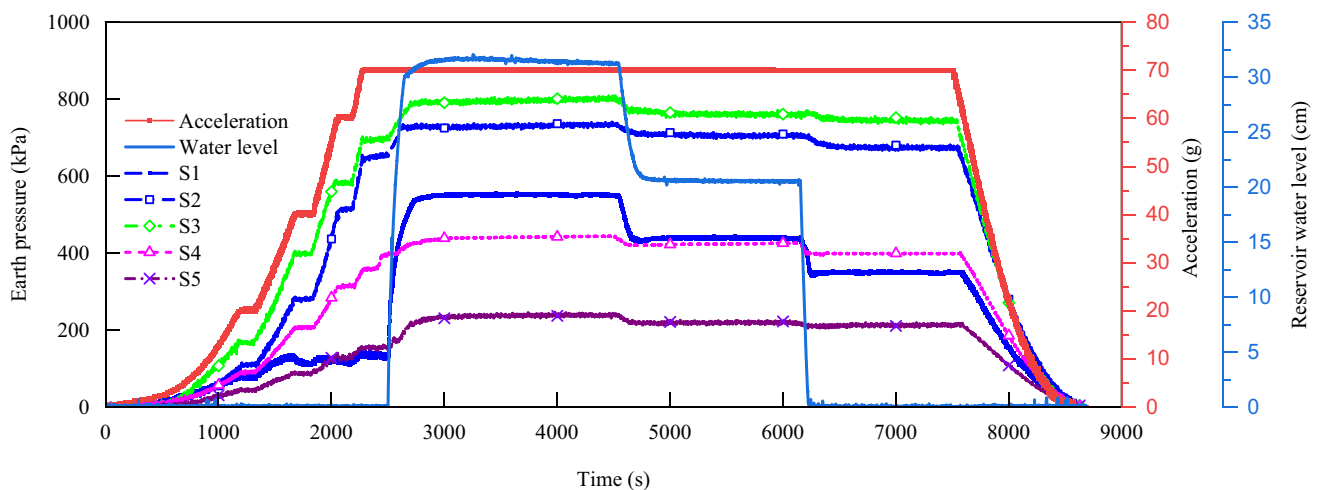


Fig. 12 Earth pressure variation curves inside the slope during the complete centrifuge modeling stage

shallowest and has the largest deformation. It shows that the larger the landslide deformation is, the smaller the deep earth pressure is. At 2520 s, the front of the slope starts to store water, and the S1 at the deep part of the front edge of the slope foot increases sharply. This increase may be attributed to water infiltrating the leading edge of the slope. Additionally, earth pressure sensors S2 and S3, positioned in the deeper sections, exhibit a slight increase due to the formation of additional pressure on the slope resulting from the hydrostatic pressure of the added reservoir water. The infiltration of reservoir water leads to the accumulation and compaction of soil in the upper portion of the slope, subsequently improving slope stability and increasing the earth pressure in this area. The earth pressure S1 drops sharply from 4561 to 4732 s and from 6241 to 6365 s because the hydrostatic pressure gradually dissipates with the sudden drop of water level during the sudden drop of reservoir water. The back pressure on the slope body decreases accordingly, and the front edge of the slope undergoes creep deformation, cracks, and slips. The slope body stress is released, and the earth pressure decreases. However, the earth pressures S2 and S3 both decrease slightly, indicating that the deformation of the position is small and the dynamic equilibrium state is maintained. During the deceleration and shutdown stage of the centrifuge, the centrifugal acceleration decreases, and the earth pressure is gradually released and finally drops to zero.

(2) Earth pressures in the middle and rear of the slope (S4 and S5).

At a loading of 70 g, S4 exhibits an increase that is 1.9 times larger than that of S5. This indicates that the deformation of soil significantly affects the shallow earth pressures in the middle and rear portion of the landslide, whereas the impact is less pronounced in the deep layer. After adding water, additional back pressure induced by hydrostatic pressure is applied on the slope, resulting in the litter increase of earth pressures at S4 and S5. The deceleration of S4 between 6241 and 6365 s is notably

more pronounced than that between 4561 and 4732 s, primarily influenced by the sudden drop rate of reservoir water. In contrast, the decline in S5 between 4561 and 4732 s is slightly greater than that between 6241 and 6365 s, predominantly influenced by the landslide deformation. These findings indicate the presence of minute cracks or deformations in the landslide body at this time, and the 2nd drop of reservoir water aggravates the expansion of the cracks or deformations.

In summary, during the rapid decrease in reservoir water level, it is evident that the changes in earth pressure are notably less pronounced compared to the variations in pore water pressure. This observation underscores the fundamental factors driving slope instability, including the softening effect, buoyancy, and dynamic water pressure within the slope's surface and internal regions. Deformation initiates with localized instability and progresses backward gradually until the entire front edge becomes unstable. In contrast, minimal variations in soil pressure are observed in the deep sections of the rear edge. This suggests that in the case of gravitational-type sliding in slope masses, a "tongue-shaped" circular slip surface is typically formed rather than an initial rock surface that results in overall sliding. Furthermore, during the accelerated deformation phase of the slope, pore water pressure and earth pressure exhibit frequent and anomalous fluctuations. These fluctuations can be considered as precursors to slope instability, providing valuable indicators for landslide prediction and early warning.

Water content variation

After the test, soil samples were taken in layers along the middle longitudinal section of the slope, and the moisture content of soil samples at different elevations and positions was measured. A total of 20 soil samples were collected, and the coordinates of each sampling point and the corresponding moisture content are shown in Table 4. According to the

Table 4 Coordinates of each sampling point and corresponding water content

Number	Coordinate (cm)	Water content (%)	Number	Coordinate (cm)	Water content (%)
1-1	(15.0, 54.5)	11.57	5-3	(45.0, 34.5)	15.57
2-1	(15.0, 49.5)	11.83	6-1	(30.0, 29.5)	14.56
2-2	(30.0, 49.5)	12.07	6-2	(45.0, 29.5)	15.94
3-1	(15.0, 44.5)	12.19	6-3	(60.0, 29.5)	16.27
3-2	(30.0, 44.5)	12.27	7-1	(50.0, 24.5)	16.37
4-1	(15.0, 39.5)	12.56	7-2	(60.0, 24.5)	16.64
4-2	(30.0, 39.5)	13.87	7-3	(80.0, 24.5)	18.12
4-3	(45.0, 39.5)	15.02	8-1	(60.0, 19.5)	17.18
5-1	(15.0, 34.5)	13.67	8-2	(80.0, 19.5)	18.57
5-2	(30.0, 34.5)	14.15	9-1	(80.0, 14.5)	19.13

measurement results, the water content distribution of the model after the test is drawn, as shown in Fig. 13.

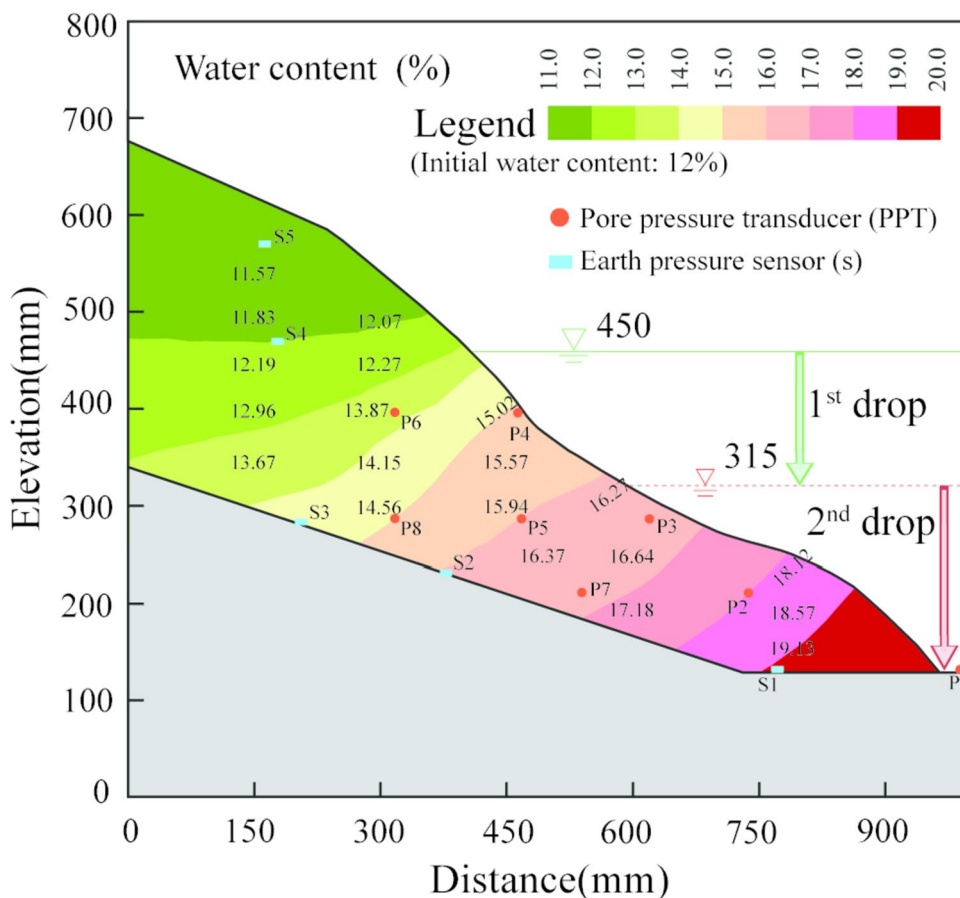
The water content increases with depth, and the change range of the water content in the water level sudden change area is larger than that in the upper part. Specifically, the water content in the region of sudden water level changes shows an approximately 1% variation from shallow to deep, while the water content in the upper part is more than 2%. Furthermore, the water content decreases as the distance from the reservoir bank increases, and this phenomenon is more pronounced in the area of sudden water level changes. Additionally, the water content of pore pressure P4, P6 and the overlying soil is relatively low, while the relative initial water content increases by approximately 1 to 1.8%. This can be attributed to the air-drying effect on the surface of the slope during the test. The soil-water content below the P4 and P6 positions is higher, ranging from 13.4 to 19.4%, with a maximum increase of 7.4% in terms of relative initial water content. In addition, the infiltration direction of the reservoir water in the low water level area has an obvious inclination angle. In the area near the high-water level, the infiltration direction gradually tends to be horizontal due to the weak intensity of reservoir water action. According to the water content

distribution map of the slope after the test, the front part deforms and collapses in a concave shape, and the soil accumulates at the slope foot to form a new stable state.

Numerical simulations

The previous section involved conducting a centrifugal modeling test under the two-step drop of reservoir water level. It was found that the magnitude of the sudden drop rate significantly affects the deformation of the reservoir bank slope. Therefore, further analysis is necessary to investigate the evolution of deformation and stability under conditions involving a two-step drop with different drop rates. A numerical simulation model with a scale of 70:1 centrifugal modeling test is developed using Geo-Studio 2012 software. The physical and mechanical parameters of the accumulation body are consistent with the centrifugal test. Subsequently, the seep/w module is used to analyze the seepage field of the slope under different operating conditions, and the seepage analysis results are imported into the sigma/w module to ascertain the stability change law.

Fig. 13 Distribution of water content of landslide at the end of the test



Calculation theories

The accumulation body above the reservoir water level remains unsaturated, while below the reservoir water level, it becomes saturated. As the reservoir water level drops, the pore water pressure in the slope gradually dissipates, leading to a transition of the soil from a saturated to an unsaturated state. However, the movement of soil water in the unsaturated area and the movement of water in the saturated area are interrelated, and the two are unified, giving rise to the well-known saturated and unsaturated problem (Vauclin et al. 1979). Based on Darcy's law, the governing equation of unsaturated seepage can be expressed as follows (Fredlund and Rahardjo 1993):

$$\frac{\partial}{\partial x} \left(k_x \frac{\partial H}{\partial x} \right) + \frac{\partial}{\partial y} \left(k_y \frac{\partial H}{\partial y} \right) + Q = \gamma_w \frac{\partial \theta_w}{\partial \psi} \frac{\partial H}{\partial t} \quad (10)$$

where k_x and k_y are hydraulic conductivity in horizontal and vertical directions, respectively. H is the total waterhead, and θ_w is volumetric water content. γ_w is the unit weight of water. ψ is the matric suction. The relationship between θ_w and ψ is the so-called soil–water characteristic curve (SWCC). Therefore, as long as the SWCC and hydraulic conductivity of the soil are known, and clear boundary conditions and initial conditions are given, the seepage field of unsteady unsaturated soil can be obtained.

The strength of unsaturated soil adopts Fredlund's two-variable strength theory. Fredlund et al. (1978) concluded through a large number of experimental data that the shear strength equation of unsaturated soil can be expressed as an independent stress variable as follows:

$$\tau_f = c' + (\sigma - u_a) \tan \varphi' + (u_a - u_w) \tan \varphi^b \quad (11)$$

where τ_f is the shear strength of the soil. c' and φ' are effective shear strength parameters. σ is normal stress. u_a and u_w are pore air and water pressures, respectively. φ^b is the frictional angle caused by matric suction.

When using the limit equilibrium method (LEM) to calculate the slope stability, the Morgenstern-Price method (Morgenstern and Price 1965) can accurately reveal the interaction force between soil strips without any simplification. Therefore, this method is used to analyze the stability of slopes in this study. The calculation results of σ/W are imported into the slope/W module, and the safety factor of the slope is calculated with LEM. Concerning the Chinese Standard SL386-2007 (2007), the stability factor of the Class 1 landslide should be higher than the safety factor under normal operating conditions and the coefficient control standard is 1.05.

Landslide modeling and meshing

To monitor the development and evolution of landslide pore water pressure in real time during the sudden change of reservoir water level, seven reference points corresponding to the centrifuge modeling test are set (P1 to P7, as shown in Fig. 7a). At the same time, when dividing the model mesh, considering the calculation accuracy and the difficulty of convergence, this paper adopts the method of mixing triangular elements and quadrilateral elements. The minimum element size of the model is controlled at 0.5 m, and it is divided into 8139 elements and 8295 nodes. The meshing of the landslide model is shown in Fig. 14.

The bottom of the landslide is fully restrained; that is, the horizontal displacement and vertical displacement are limited. Horizontal displacement constraints are imposed on both sides of the model; that is, the water level displacement is limited. The fixed water head boundary on the left side of the model is set to be 20 m, and the front slope surface is the water head boundary of the reservoir water level. The slope table of the front edge of the model is set as the boundary of the sudden change in reservoir water level. It changes according to the variation of the water level of the reservoir under each working condition, and other boundaries are set as impervious boundaries.

According to the results of the geological survey and laboratory test, the physical and mechanical parameters of the landslide mass, sliding surface, and slip bed are the same as the centrifuge modeling test (Table 5).

Knowing the saturated volumetric water content of different materials of the landslide body, the soil–water characteristic curve (SWCC) and the relationship curve between the permeability coefficient and matrix suction of the landslide body can be estimated and plotted using the Fredlund et al. (1996) model function, as shown in Figs. 15 and 16, respectively.

Validation of the model

Through a similar relationship to the centrifugal modeling test, the pore pressure values of the sensors' corresponding positions are extracted in the numerical simulation to compare the accuracy of the test with the numerical simulation, as shown in Fig. 17.

It can be seen from Fig. 17 that all sensor points are positioned above the groundwater infiltration line. Consequently, the initial pore water pressure is negative due to the influence of liquid surface tension (Rinaldi and Casagli 1999). As the reservoir water level rises, pore pressures at P2 and P7 respond first, succeeded by pore pressures P3, P5, and

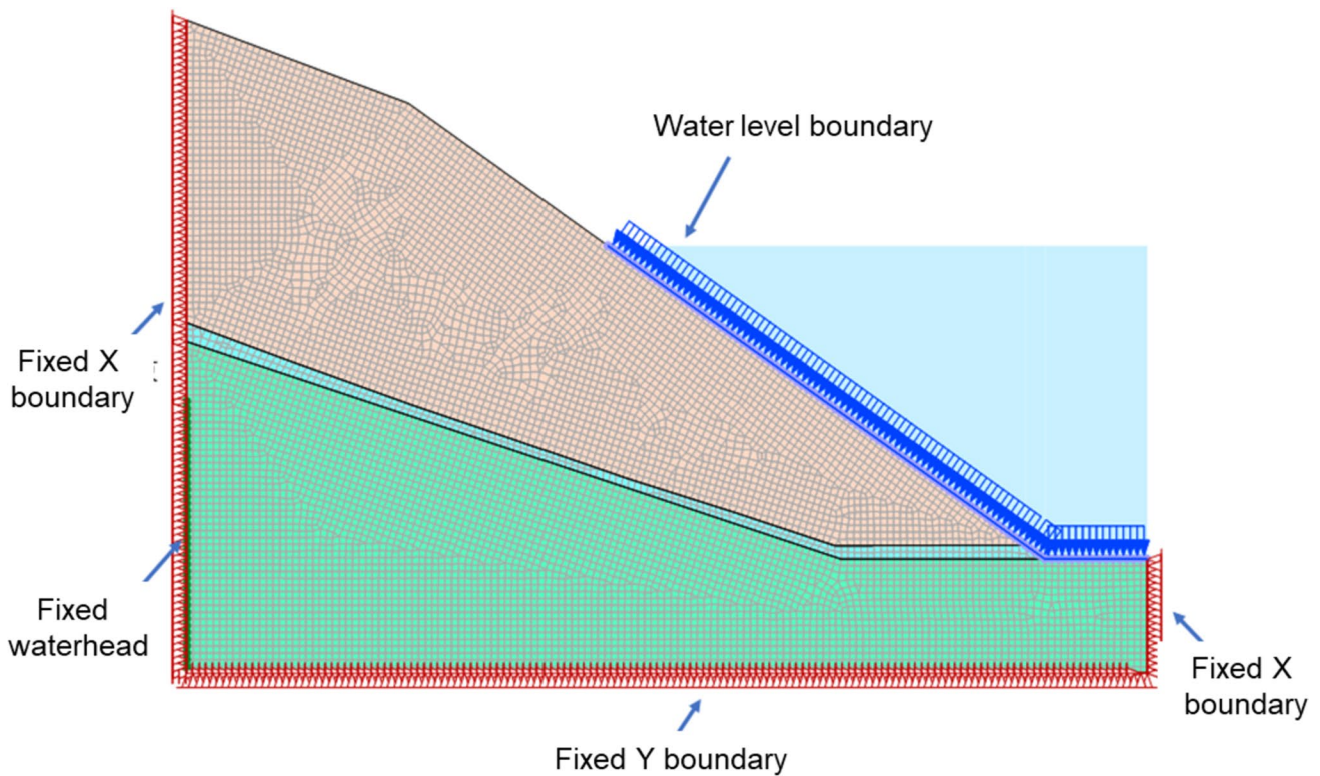


Fig. 14 Landslide model mesh sectioning

Table 5 Physical and mechanical parameters of the landslide in the simulation model

Parameters	Landslide mass	Sliding surface	Slip bed
Permeability coefficient k_{sat} (m/d)	6.05	7.76	0.05
Unit weight γ_{sat} (kN/m ³)	20.4	21.9	22.7
Effective cohesion c' (kPa)	12.1	13.4	16.7
Effective frictional angle φ' (°)	13.2	14.9	16.8
Frictional angle caused by matric suction φ^b (°)	10	10	10
Saturated volume moisture content θ_s	0.26	0.21	0.05

P8, and eventually P4 and P6. Nevertheless, the time interval of pore pressure response is shortened during the 1st drop stage and becomes less discernible after the subsequent drop. This indicates that there exists hysteresis in the pore pressure response to variations in the reservoir water level, and such hysteresis gradually diminishes with the two-step drop. The pore pressure in the lower part of the slope has the swiftest response, succeeded by the middle section, whereas the upper section experiences the slowest response. Because the sensors P2, P3, and P4 are close to the slope, their changes are more sensitive than those of the P5, P6, P7, and P8. The numerical simulation result of pore water pressure is obtained by unsaturated seepage theory, representing the seepage field under ideal conditions. A comparison between the results of the centrifugal modeling test (Fig. 11)

and numerical simulation (Fig. 17) reveals similar seepage fields, but some differences exist. In summary, the differences are as follows.

- (1) The pore pressure sensors used in the centrifugal test can only measure positive pore water pressure; there is no negative pore pressure like that in the numerical simulation.
- (2) Pore water pressure is influenced not only by water content and infiltration line but also by the properties of soil materials. The model test results of the pore pressure sensors near the reservoir bank are higher, while in the numerical simulation, the monitoring points at the same elevation are the same. One possible explanation is that the voids between soil particles are filled with

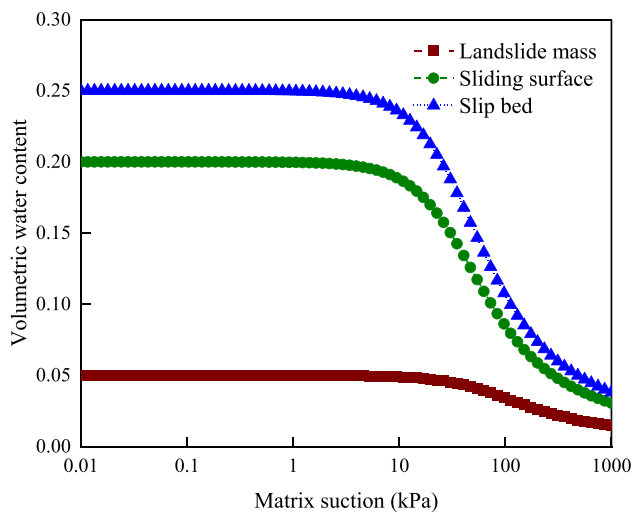


Fig. 15 Volumetric water content-matrix suction relationship curve

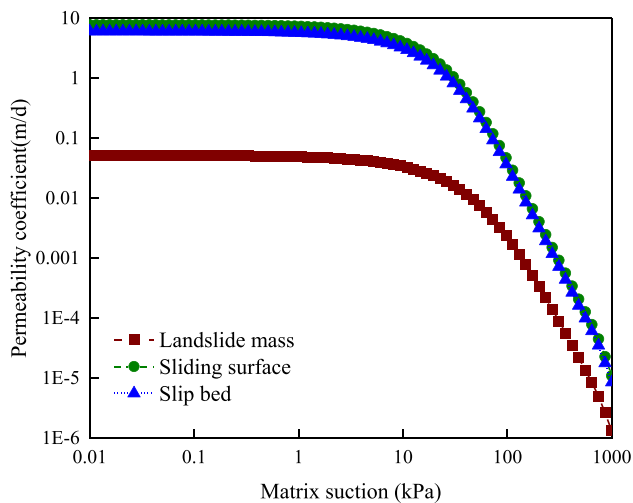


Fig. 16 Permeability coefficient-matrix suction relationship curve

water and small soil particles near the bank. On the other hand, the positions of the pore pressure sensor have changed during the landslide deformation process, which makes the measured values deviate. The further downward its position is, the more obvious the deviation is.

- (3) During the centrifugal model test, numerous cracks appeared in the front, middle, and rear of the slope, altering the slope soil's permeability and causing changes in pore water pressure.

To compare the difference in the water content of the landslide model, the volumetric water content at the last step of the numerical simulation of the landslide model was extracted, as shown in Fig. 18.

The differences between the numerical simulation and laboratory tests are evidently significant when compared with the test results. The reasons for these differences are as follows: Firstly, slope deformation alters the permeability of the original slope soil, resulting in a discrepancy between the infiltration state of the reservoir water and the numerical simulation seepage state. Secondly, due to the expansion of multiple cracks at the leading edge during the centrifugal test, the groundwater seepage speed is accelerated, resulting in lower water content at the far bank end of the slope. However, the numerical simulation fails to accurately reflect this process.

Effects of different reservoir level drop rates on landslides

Even though the numerical simulation method has the aforementioned drawbacks, using qualitative analysis, it is still possible to determine the influence of the law of water level drop rate on slope stability. It can be seen from the previous centrifugal test and numerical simulation that the 1st drop rate influences the deformation significantly due to the high reservoir water level. It is very easy to cause deformation and damage to the slope. Therefore, it is necessary to further explore the seepage change and stability of the slope under the condition that the 1st drop rate of the reservoir water level is inconsistent.

The reservoir water level of the Huangdeng Hydropower Station in the Lancang River dropped by 33 m from April to June. However, due to the limitation of the size of the centrifuge device and the test conditions, the centrifugal model test simulated the rise and two-step drop of the reservoir water level at the front edge of the slope with a height of 23.1 m. Among them, the drop rate in the two-step drop stage of the reservoir water level adopts the pattern of slow first and then fast, which is consistent with the actual engineering. From the test results, the sudden drop rate of the reservoir water level that causes the deformation and instability of the slope is 0.7~1.5 m/d. To further clarify the critical value of the reservoir water level drop rate that induces slope instability, three reservoir water level drop conditions are set up in this study. Among them, to ensure that the rising stage of the reservoir water level is consistent with the experimental conditions, the rising rates are all set to 2.0 m/d. The 1st drop rates are set as 0.7 m/d, 1.1 m/d, and 1.5 m/d, respectively, while the 2nd drop rate is controlled at 1.5 m/d. The specific operation conditions are shown in Fig. 19.

The pore pressure variation curves of the sensor coordinate points under three operation conditions were extracted and shown in Fig. 20. The farther from the reservoir bank and the lower the position of the sensor coordinate point,

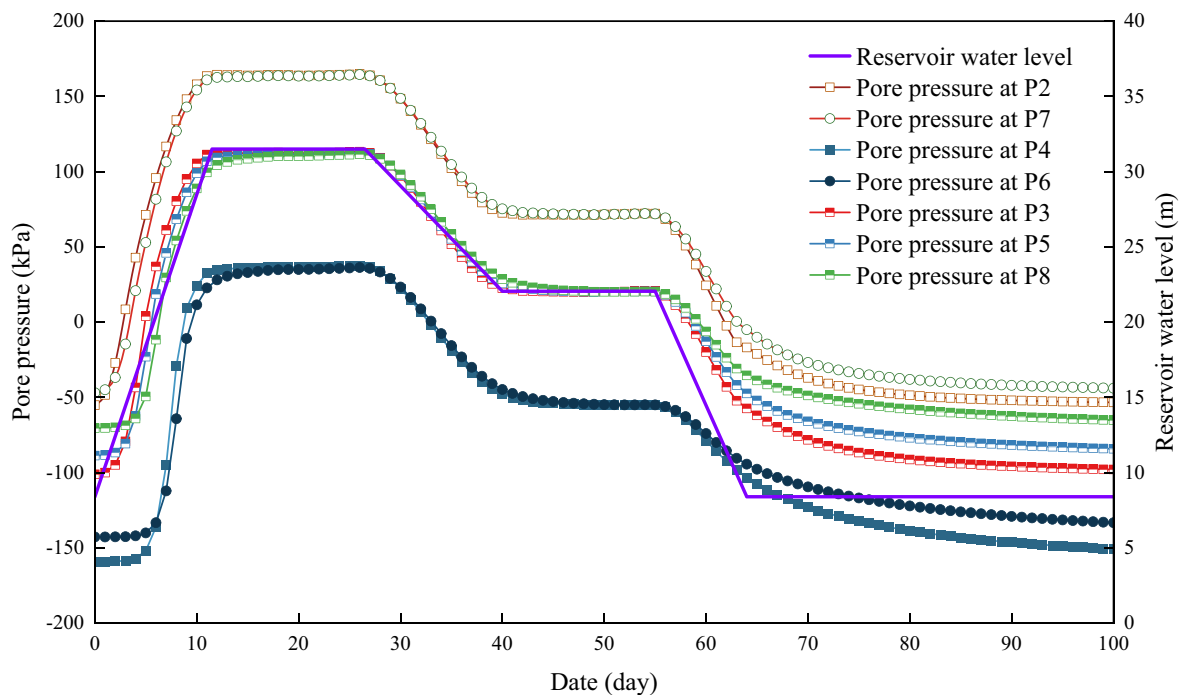
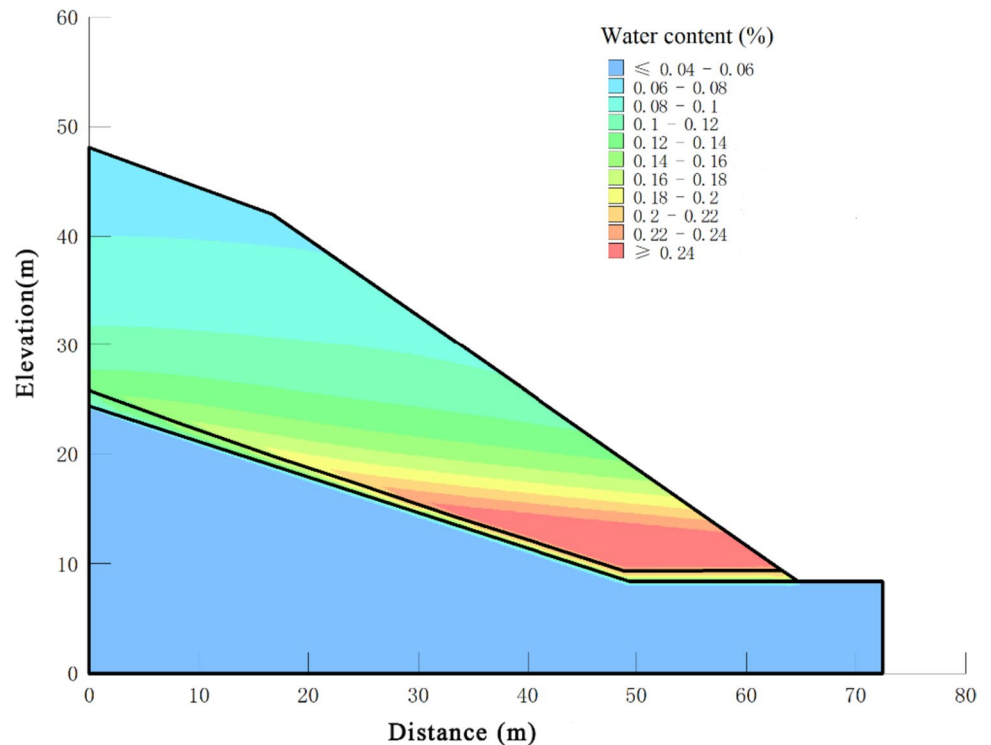


Fig. 17 Numerical simulation results of pore water pressure variation at sensor points corresponding to the centrifugal modeling test

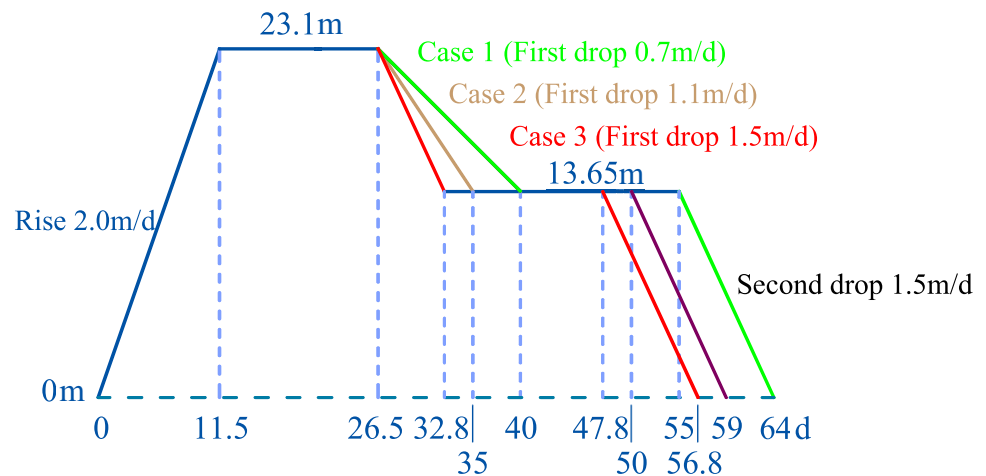
Fig. 18 Contour plot of the volumetric water content of landslide model at the end of numerical simulation



the more lag the pore pressure response. It also takes longer for the pore pressure to stabilize. The hysteresis of the pore pressure caused by the height of the position is more obvious than that of the distance from the reservoir bank.

During the 1st drop of reservoir water level, the drop rate of pore pressure P2 and P7 is significantly higher than that of P3, P5, P8, P4, and P6 under the condition of a 1.5 m/d drop rate. However, the drop rates of P2 and P7 are slightly higher

Fig. 19 Calculated working condition setting diagrams



than those of P3, P5, P8, P4, and P6 under the condition of a 0.7 m/d drop rate. It shows that the greater the velocity in the 1st drop, the faster the pore pressure at the front edge of the landslide decreases, the stronger the hydrodynamic pressure effect, and the less conducive to the safety and stability of the slope. In the 2nd drop stage, the rate of 1.5 m/d has little effect on the different failure stages of the slope.

Stability analysis

The variation of the factor of safety (FOS) of the three conditions is shown in Fig. 21. From 0 to 11.5 days, the front edge is affected by the hydrostatic pressure of the reservoir water during the reservoir impoundment stage, and the stability increases rapidly (Song et al. 2017). From 11.5 to 26.5 days, the reservoir water level is stable at 31.5 m. Due to the low permeability coefficient of the accumulation body, the change of the groundwater level in the slope lags behind the sudden rise of the reservoir water level, so the groundwater level continues to rise during this period. The slope front changes from natural bulk density to floating bulk density, resulting in a slight decrease in the stability coefficient during this period.

During the 1st drop stage, the dynamic water pressure points to the outside of the slope, which adversely affects the stability. When the drop rate is 0.7 m/d (case 1), the stability coefficient decreases almost uniformly. By day 40, the FOS drops to 1.41. When the drop rate is 1.1 m/d (case 2), the decrease rate of the FOS is significantly faster than that in case 1. By day 35, the FOS drops to 1.29. When the drop rate is 1.5 m/d (case 3), the FOS decreases sharply. By 32.8 days, the value decreases to 1.20. During the stable period after the 1st drop, the groundwater further seeps out of the slope under the dynamic water pressure because the change of the groundwater infiltration line lags behind the sudden drop of the reservoir water level. The landslide

infiltration line decreases, and the head difference between the reservoir water level and the infiltration line increases, increasing the dynamic water pressure pointing to the slope. Therefore, the FOS recovers slightly.

There is no significant difference in the decline range of the FOS among the three working conditions in the 2nd drop stage, and the decline range is significantly smaller than that in the 1st drop stage. This is because the reservoir water level in this period is lower than that in the previous stage, and the effect of hydrodynamic pressure is weakened. In case 1, the reservoir water level drops sharply by 1.5 m/d during this period, and on the 64th day, the FOS drops to 1.22. From case 2 to day 59, the FOS drops to 1.09. On the 56.8th day of case 3, the FOS decreases to 0.99, which is less than 1.05. It can be seen that the FOS of the accumulation body under this working condition is the smallest, and instability is very likely to occur, which is the most unfavorable working condition under the reservoir water level adjustment.

The above analysis shows that the FOS is most sensitive when the 1st drop rate is 1.5 m/d. The minimum stability factor is lower than the normal operating conditions stipulated in Chinese standard SL386-2007 (2007). In addition, the minimum FOS is also much closer to the control standard of the safety factor when the 1st drop rate is 1.1 m/d. Therefore, the 1st drop rate that causes landslide deformation and instability is 1.1–1.5 m/d.

Discussion

Reservoir storage and subsequent changes in water levels often serve as triggers for bank landslides (Gutiérrez et al. 2010; Schuster 1979; Tang et al. 2019). However, it is crucial to recognize that the influence of reservoir water on different types of landslides can vary significantly (Qi et al. 2006). For example, Jones et al. (1961) reported that nearly 49% of

Fig. 20 Numerical simulation of pore water pressure changes at sensor coordinates for the 1st drop rate of (a) 0.7 m/d, (b) 1.1 m/d, and (c) 1.5 m/d

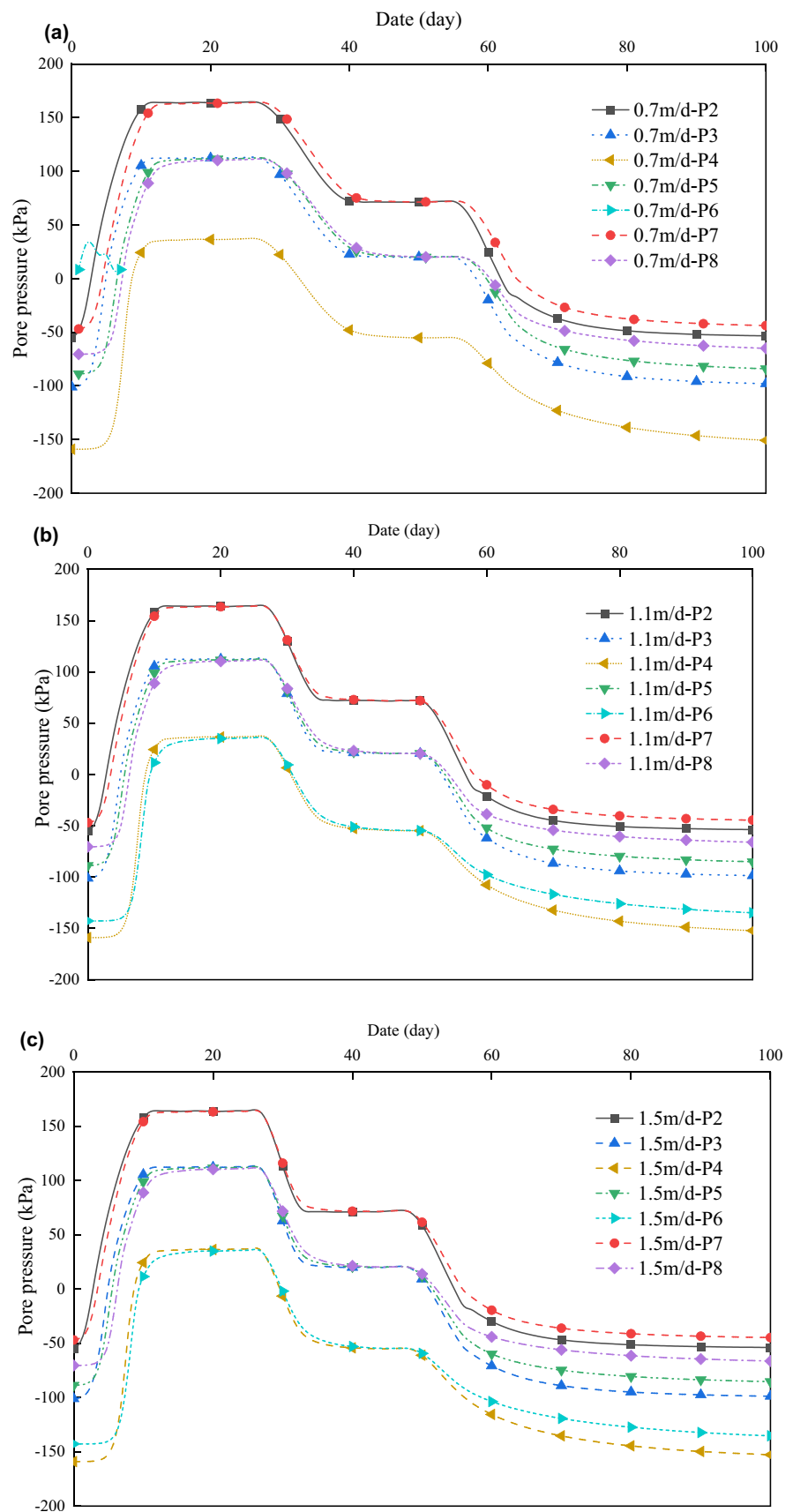
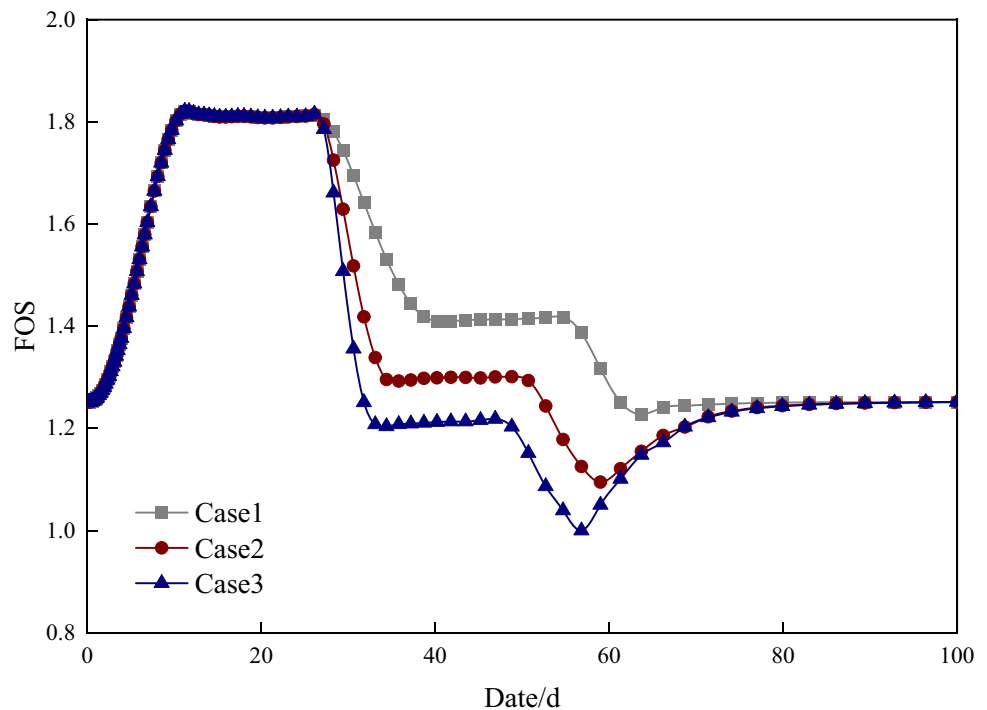


Fig. 21 FOS variation curve of the three working conditions



the landslides in the vicinity of Roosevelt Lake, occurring between 1941 and 1953, took place during the early stage of impoundment from 1941 to 1942, while approximately 30% occurred when the water level rapidly dropped by 10 to 20 m. The rest are small landslides that occurred at other times. About 60% of reservoir landslides in Japan occur during periods of sudden reservoir water levels. The remaining 40% occurred during periods of rising water levels, including the early stages of impoundment. Some landslides occurred during the reservoir storage period, and some landslides occurred during the reservoir water level drop (Nakamura 1990). The physical trigger mechanism behind this well-known relationship between water and landslides is a reduction in shear strength due to buoyancy exerted by water in saturated soils and a reduction in soil suction in unsaturated soils (Mazaeva et al. 2019; Záruba and Mencl 2014). The schematic diagram of the landslide in the accumulation body triggered by a two-step drop in reservoir water level is shown in Fig. 22. In this study, through the analysis of the deformation process of the sliding body in the reservoir impoundment stage, the front edge of the slope is continuously softened by water immersion. However, the floating force formed by the groundwater staying in the slope body and the seepage pressure of the reservoir water on the slope body offset each other, so there is no obvious deformation of the slope in this stage (Fig. 22b). In addition, the high consolidation strength of the accumulation body in the Huangdeng reservoir area and the occlusal effect of soil and stone in the landslide body also inhibit the sliding of the slope. Due to the differences in landslide geological structure and slope morphology, the

influence characteristics of reservoir water level fluctuation on landslide stability also show different forms, including seepage-driven type and buoyancy-driven type (Zhou et al. 2022). The term “seepage-driven landslide” describes a landslide that underwent significant deformation as a result of the hydrodynamic pressure effect (also known as the “seepage force”) or when the landslide’s topography and geological structure are susceptible to the hydrodynamic pressure. The term “buoyancy-driven landslide” describes a landslide that underwent significant deformation as a result of the buoyancy force effect or a slope whose topography and geological structure are particularly susceptible to the unloading effect brought on by buoyancy force.

Through the model test and numerical simulation, it is found that in the early stage of the 1st drop of the water level, when the water level of the reservoir suddenly drops, the pore water pressure is difficult to dissipate, resulting in an outward seepage force. Under the traction of the sliding force of the slope body, the softened accumulation body undergoes creep deformation, which leads to the formation of tensile cracks in the front of the sliding body (Fig. 22c). At the same time, tension cracks are generated in the middle and rear sections of the slope under the traction of the front deformation body. However, in the middle and late stages of the first sudden drop in water level, the seepage effect is enhanced, and the tensile cracks on the front edge further expand and penetrate laterally and deep under the action of strong hydrodynamic pressure. As a result, the lower staggered slump takes place, and the tensile cracks in the middle and back of the traction landslide keep growing. This

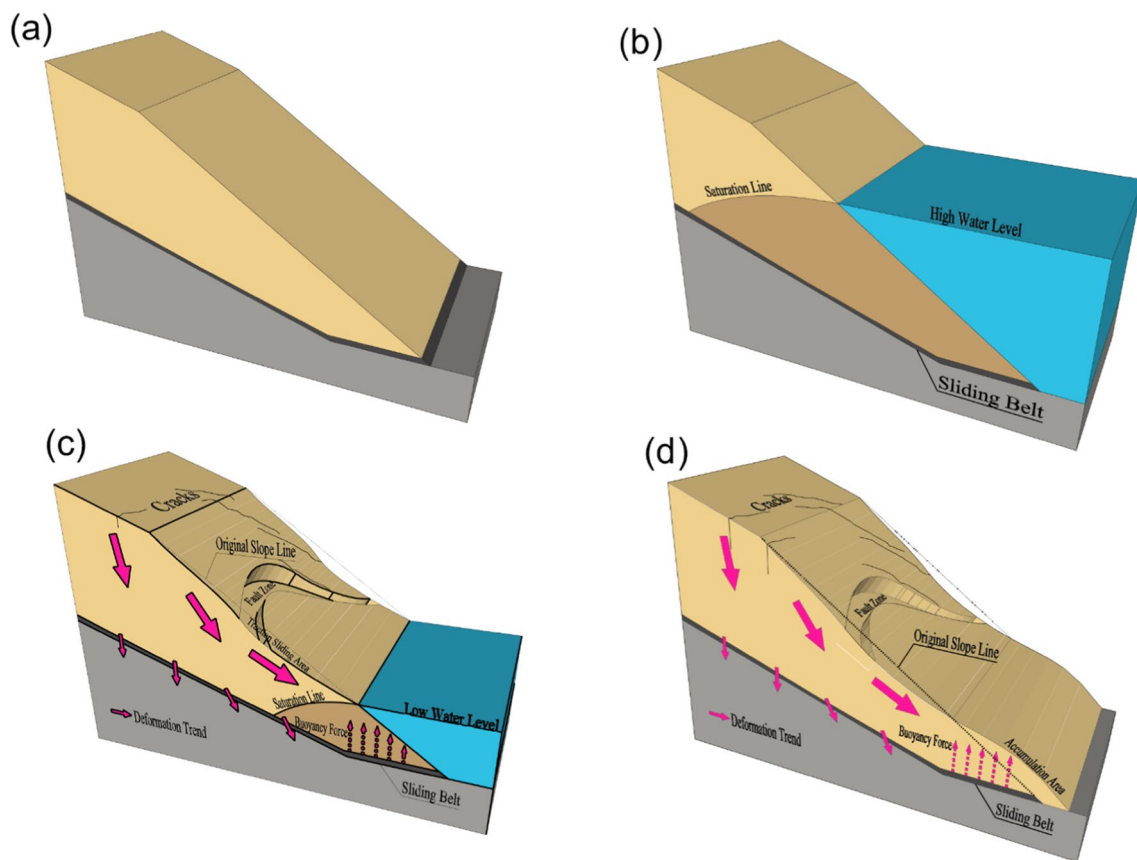


Fig. 22 Schematic diagram of the landslide deformation evolution model in Huangdeng reservoir: (a) initial reservoir bank slope, (b) deformation of slope after impoundment, (c) deformation during the 1st water level drop stage, and (d) deformation during the 2nd water level drop stage

exhibits the traits of traction failure, in which the deformation gradually deteriorates from the front edge to the back section.

During the 2nd drop stage, the sliding mass continued to move along the fractured fault zone, rendering the slope as a whole unstable. However, the sliding is less pronounced compared to the 1st drop, and the extension of tension cracks in the middle and rear parts is weak (Fig. 22d). This is because the start-up water level is low at this time, and the intensity of groundwater seepage is still low even if the water level drop rate doubles. In addition, the first slip created a seepage channel, thereby reducing the degree of hysteresis in the deep part of the slip. Therefore, the hydrodynamic pressure effect of the 2nd drop is weaker than that of the 1st drop. Throughout the entire testing process, the deformation of the sliding body exhibits the characteristics of attenuation deformation from initial deformation to accelerated deformation to deceleration deformation.

The middle and rear parts of the slope exhibit vertical deformation and compaction, which enhances the anti-sliding ability of this part, resulting in relatively small deformation. In general, the range of water level drop rate that causes instability of the landslide model is 3.4–7.3 cm/min,

corresponding to a water level dip rate range of the prototype landslide 0.7–1.5 m/d. The hysteresis degree of the slope deformation during the rise and fall of the reservoir water follows this order: water level rising stage > the 1st drop of the water level > the 2nd drop of the water level. For the continuous sudden drop of water level, the landslide deformation is greatly affected by the 1st drop of water level even if the drop rate is smaller. Therefore, the landslide in Huangdeng Reservoir belongs to the seepage-driven type.

Conclusion

To study the deformation and evolution mechanism of reservoir bank slope triggered by a fast two-step drop in water level, a 1:70 slope model was established with a typical accumulation body in the Huangdeng Reservoir area as the prototype, and a reservoir water level rise and fall system was designed. Centrifugal modeling tests of one water level rise and two-step drop at different rates were carried out. Based on the test results, a numerical simulation was conducted to analyze the critical drop rate on the deformation of the slope. The main results are as follows.

- (1) Landslide deformation characteristics show the form of small deformation to large deformation and then weakening deformation during the complete test process. At the stage of reservoir impoundment, the slope deformation is small. At the 1st drop stage, the cracks at the leading edge propagate under the strong dynamic water pressure, and tensile cracks appear at the middle and rear of the traction. At the 2nd drop stage, the extension of the fracture zone is weakened, and the whole slippage occurs at the leading edge.
- (2) The pore pressure and earth pressure monitoring data show that the slope undergoes multiple deformation processes. Specifically, settlement deformation occurs during the impoundment stage, whereas overall slippage is observed during the water level drop process. The water content in the area of a sudden change of water level is higher, while the increase of water content in the middle and rear part of the slope is not significant.
- (3) The numerical simulation results indicate that a higher 1st drop rate leads to a larger hydraulic gradient both inside and outside the slope, a more rapid downward movement of the pore water pressure contour, increased hysteresis of groundwater, and a larger decline rate of the infiltration line. The FOS increases during the reservoir impoundment stage and stabilizes between the two drop stages. Moreover, a higher drop rate during the 1st drop stage corresponds to a greater decrease rate of FOS. The decreased rate of FOS in the 1st drop stage is higher than that in the 2nd drop stage, even though the drop rate in the 2nd stage is much higher.
- (4) The primary cause of the slope deformation under the condition of a two-step drop in water level is the infiltration of water into the slope, leading to a reduction in the shear strength of the soil body. During the 1st drop stage, stability decreases significantly. In the 2nd drop stage, the dynamic water pressure continues to be released, and the deformation of the leading edge of the slope increases, showing the characteristics of traction-type damage. The two successive drops of the reservoir water level leading to the instability of the accumulation body in Huangdeng Reservoir bank are mainly the 1st drop with a rate between 1.1 and 1.5 m/d.

Acknowledgements The work presented in this paper was financially supported by the Open Research Fund of the State Key Laboratory of Simulation and Regulation of Water Cycle in River Basin (China Institute of Water Resources and Hydropower Research) (No. IWHR-SKL-KF202016), the National Key R&D Program of China (No. 2017YFC1501100), the IWHR Research program (No. GE110145B0012023), and the Central South University Autonomous Exploration Project (No. 2021zzts0233).

Data availability All data, models, and codes that support the findings of this study are available from the corresponding author upon reasonable request.

Declarations

Conflict of interest The authors declare no competing interests.

References

- Askarinejad A, Springman SM (2015) Centrifuge modelling of the effects of vegetation on the response of a silty sand slope subjected to rainfall. *Computer Methods and Recent Advances in Geomechanics: Proceedings of the 14th International Conference of International Association for Computer Methods and Recent Advances in Geomechanics, 2014 (IACMAG 2014)*. Taylor & Francis Books Ltd, 1339–1344
- Chen H, Qin S, Xue L, Xu C (2021) Why the Xintan landslide was not triggered by the heaviest historical rainfall: mechanism and review. *Eng Geol* 294:106379. <https://doi.org/10.1016/j.enggeo.2021.106379>
- Dong M, Kulatilake PHSW, Zhang F (2018) Deformation and stability investigations in 3-D of an excavated rock slope in a hydroelectric power station in China. *Comput Geotech* 96:132–149. <https://doi.org/10.1016/j.compgeo.2017.10.019>
- Du Y, Zhu S, Liu L, Han L (1992) Development of LXJ-4–450 centrifuge for geotechnical engineering. *Shuili Xuebao* 2(19):28. <https://doi.org/10.13243/j.cnki.slxu.1992.02.003>
- Eab KH, Takahashi A, Likitlersuang S (2014) Centrifuge modelling of root-reinforced soil slope subjected to rainfall infiltration. *Geotechnique Lett* 4:211–216. <https://doi.org/10.1680/geolett.14.00029>
- Fredlund DG, Morgenstern NR, Widger RA (1978) The shear strength of unsaturated soils. *Can Geotech J* 15:313–321. <https://doi.org/10.1139/t78-029>
- Fredlund DG, Rahardjo H (1993) *Soil mechanics for unsaturated soils*. Wiley
- Fredlund DG, Xing A, Fredlund MD, Barbour SL (1996) The relationship of the unsaturated soil shear strength to the soil-water characteristic curve. *Can Geotech J* 33:440–448. <https://doi.org/10.1139/t96-065>
- Fuglsang LD, Ovesen NK (1988) The application of theory of modelling to centrifuge studies. In: Craig WH, James RG, Schofield AN (eds) *Centrifuge in soil mechanics*. Balkema, Rotterdam
- Ge S, Zu-yu C, Yuan L, Ming-shou Z, Jian-yu W (2017) Experimental and numerical investigation of the centrifugal model for underwater explosion shock wave and bubble pulsation. *Ocean Eng* 142:523–531. <https://doi.org/10.1016/j.oceaneng.2017.04.035>
- Gue CS, Soga K, Bolton MD, Thusyanthan NI (2010) Centrifuge modelling of submarine landslide flows. In: *Proceedings of the 7th International Conference on Physical Modelling in Geotechnics 2010*, vol 2. ICPMG 2010, pp 1113–1118
- Gutiérrez F, Lucha P, Galve JP (2010) Reconstructing the geochronological evolution of large landslides by means of the trenching technique in the Yesa Reservoir (Spanish Pyrenees). *Geomorphology* 124:124–136. <https://doi.org/10.1016/j.geomorph.2010.04.015>
- Highland L, Bobrowsky PT (2008) *The landslide handbook: a guide to understanding landslides*. US Geological Survey Reston, Reston, Virginia, U.S
- Huang B, Yin Y, Wang S, Tan J, Liu G (2017) Analysis of the Tangji-axi landslide-generated waves in the Zhexi Reservoir, China,

- by a granular flow coupling model. *Nat Hazards Earth Syst Sci* 17:657–670. <https://doi.org/10.5194/nhess-17-657-2017>
- Idinger G, Aklík P, Wu W, Borja RI (2011) Centrifuge model test on the face stability of shallow tunnel. *Acta Geotech* 6:105–117. <https://doi.org/10.1007/s11440-011-0139-2>
- Jia C, Zhang S, Xu W (2021) Experimental investigation and numerical modeling of coupled elastoplastic damage and permeability of saturated hard rock. *Rock Mech Rock Eng* 54:1151–1169. <https://doi.org/10.1007/s00603-020-02319-5>
- Jones FO, Embody DR, Peterson WL (1961) Landslides along the Columbia River Valley. Government Printing Office, Northeastern Washington. U.S
- Liu HD, Chen JX, Han WX, Wu Y, Li DD (2022) Centrifuge model tests and numerical simulations of the landslide evolution process. *KSCE J Civ Eng* 26:2588–2599. <https://doi.org/10.1007/s12205-022-0664-6>
- Mazaeva O, Babicheva V, Kozyreva E (2019) Geomorphological process development under the impact of man-made reservoir operation, a case study: Bratsk reservoir, Baikal-Angara hydroengineering system, Russia. *Bull Eng Geol Environ* 78:4659–4672. <https://doi.org/10.1007/s10064-018-1428-x>
- Miao FS, Wu YP, Li LW, Tang HM, Li YN (2018) Centrifuge model test on the retrogressive landslide subjected to reservoir water level fluctuation. *Eng Geol* 245:169–179. <https://doi.org/10.1016/j.enggeo.2018.08.016>
- Miao FS, Wu YP, Torok A, Li LW, Xue Y (2022) Centrifugal model test on a riverine landslide in the Three Gorges Reservoir induced by rainfall and water level fluctuation. *Geosci Front* 13:101378. <https://doi.org/10.1016/j.gsf.2022.101378>. ARTN101378
- Morgenstern NR, Price VE (1965) The analysis of the stability of general slip surfaces. *Geotechnique* 15:79–93. <https://doi.org/10.1680/geot.1965.15.1.79>
- Nakamura K (1990) On reservoir landslide. *Bull Soil Water Conserv* 10:53–64
- Paronuzzi P, Rigo E, Bolla A (2013) Influence of filling–drawdown cycles of the Vajont reservoir on Mt. Toc slope stability. *Geomorphology* 191:75–93. <https://doi.org/10.1016/j.geomorph.2013.03.004>
- Pinyol NM, Alonso EE, Corominas J, Moya J (2012) Canelles landslide: modelling rapid drawdown and fast potential sliding. *Landslides* 9:33–51. <https://doi.org/10.1007/s10346-011-0264-x>
- Qi SW, Yan FZ, Wang SJ, Xu RC (2006) Characteristics, mechanism and development tendency of deformation of Maoping landslide after commission of Geheyan reservoir on the Qingjiang River, Hubei Province, China. *Eng Geol* 86:37–51. <https://doi.org/10.1016/j.enggeo.2006.04.004>
- Riemer W (1992) Landslides and reservoirs. *Proceedings of the 6th International Symposium on Landslides*: 1373–2004.
- Rinaldi M, Casagli N (1999) Stability of streambanks formed in partially saturated soils and effects of negative pore water pressures: the Sieve River (Italy). *Geomorphology* 26:253–277. [https://doi.org/10.1016/S0169-555X\(98\)00069-5](https://doi.org/10.1016/S0169-555X(98)00069-5)
- Schuster RL (1979) Reservoir-induced landslides. *Bull Int Assoc Eng Geol* 20:8–15. <https://doi.org/10.1007/bf02591233>
- SL386-2007 (2007) Design code for engineerined slopes in water resources and hydropower projects. Ministry of Water Resources of the People's Republic of China, Beijing
- Song K, Lu GD, Zhang GD, Liu YL (2017) Influence of uncertainty in the initial groundwater table on long-term stability of reservoir landslides. *Bull Eng Geol Environ* 76:901–908. <https://doi.org/10.1007/s10064-016-0909-z>
- Tang HM, Wasowski J, Juang CH (2019) Geohazards in the three Gorges Reservoir Area, China Lessons learned from decades of research. *Eng Geol* 261:105267. <https://doi.org/10.1016/j.enggeo.2019.105267>. ARTN105267
- Tian JJ, Li TT, Pei XJ, Ding F, Sun H, Xie XG, Guo J (2022) Formation and reactivation mechanisms of large-scale ancient landslides in the Longwu River basin in the northeast Tibetan Plateau, China. *J Mt Sci* 19:1558–1575. <https://doi.org/10.1007/s11629-021-7261-x>
- Trzhtsinskii YB (1978) Landslides along the Angara reservoirs. *Bull Int Assoc Eng Geol* 17:42–43. <https://doi.org/10.1007/bf02634674>
- Vauclin M, Khanji D, Vachaud G (1979) Experimental and numerical study of a transient, two-dimensional unsaturated-saturated water table recharge problem. *Water Resour Res* 15:1089–1101. <https://doi.org/10.1029/WR015i005p01089>
- Wang FW, Zhang YM, Huo ZT, Matsumoto T, Huang BL (2004) The July 14, 2003 Qianjiangping landslide, Three Gorges Reservoir, China. *Landslides* 1:157–162. <https://doi.org/10.1007/s10346-004-0020-6>
- Wang F, Zhang YM, Huo ZT, Peng XM, Wang SM, Yamasaki S (2008) Mechanism for the rapid motion of the Qianjiangping landslide during reactivation by the first impoundment of the Three Gorges Dam reservoir, China. *Landslides* 5:379–386. <https://doi.org/10.1007/s10346-008-0130-7>
- Wang ZT, Zhang Y, Yu L, Yang Q (2020) Centrifuge modelling of active pipeline-soil loading under different impact angle in soft clay. *Appl Ocean Res* 98:102129. <https://doi.org/10.1016/j.apor.2020.102129>. ARTN 102129
- Wang L, Zhu B, Chen Y, Wang P, Wang X (2022) Centrifuge modelling on behaviour of hydrate bearing sediments during gas production by depressurization. 10th International Conference on Physical Modelling in Geotechnics 2022 (ICPMG2022). *Physical Modelling in Geotechnics*, Seoul, Korea
- Wang L-J, Wang P, Zhu B, Wang X-B, Yang S-Q, Chen Y-M (2023) Development and application of centrifuge in-flight apparatus for hydrate exploitation modelling. *Chin J Geotech Eng* 03(1):9
- Yilmaz I, Ekemen T, Yildirim M, Keskin I, Ozdemir G (2006) Failure and flow development of a collapse induced complex landslide: the 2005 Kuzulu (Koyulhisar, Turkey) landslide hazard. *Environ Geol* 49:467–476. <https://doi.org/10.1007/s00254-005-0113-0>
- Yin Y, Huang B, Wang W, Wei Y, Ma X, Ma F, Zhao C (2016) Reservoir-induced landslides and risk control in Three Gorges Project on Yangtze River, China. *J Rock Mech Geotech Eng* 8:577–595. <https://doi.org/10.1016/j.jrmge.2016.08.001>
- Záruba Q, Mencl V (1969) Landslides and their control. Elsevier, Amsterdam, p 205
- Zhang WY, Askarinejad A (2019) Centrifuge modelling of submarine landslides due to static liquefaction. *Landslides* 16:1921–1938. <https://doi.org/10.1007/s10346-019-01200-z>
- Zhang S, Pei XJ, Wang SY, Huang RQ, Zhang XC, Chang ZL (2019) Centrifuge model testing of a loess landslide induced by rising groundwater in Northwest China. *Eng Geol* 259:105170. <https://doi.org/10.1016/j.enggeo.2019.105170>. ARTN105170
- Zhao TL, Chen SS, Fu CJ, Zhong QM (2019) Centrifugal model tests and numerical simulations for barrier dam break due to overtopping. *J Mt Sci* 16:630–640. <https://doi.org/10.1007/s11629-018-5024-0>
- Zhou HZ, Zheng G, Liu JF, Yu XX, Yang XY, Zhang TQ (2019) Performance of embankments with rigid columns embedded in an inclined underlying stratum: centrifuge and numerical modelling. *Acta Geotech* 14:1571–1584. <https://doi.org/10.1007/s11440-019-00825-7>
- Zhou C, Cao Y, Yin KL, Intrieri E, Catani F, Wu LX (2022) Characteristic comparison of seepage-driven and buoyancy-driven landslides in Three Gorges Reservoir area, China. *Eng Geol* 301:106590. <https://doi.org/10.1016/j.enggeo.2022.106590>. ARTN 106590

Springer Nature or its licensor (e.g. a society or other partner) holds exclusive rights to this article under a publishing agreement with the author(s) or other rightsholder(s); author self-archiving of the accepted manuscript version of this article is solely governed by the terms of such publishing agreement and applicable law.